DOI: 10.1002/ ((please add manuscript number))
Article type: Full paper

Plasma Functionalized Isotactic Polypropylene Assembled with Conducting Polymers for Bacterial Quantification by NADH Sensing

Brenda G. Molina, Luis J. del Valle, Jordi Casanovas, Sonia Lanzalaco, Maria M. Pérez-Madrigal, Pau Turon, Elaine Armelin, and Carlos Alemán**

Dr. B. G. Molina, Dr. L. J. del Valle, Dr. S. Lanzalaco, Dr. M. M. Pérez-Madrigal, Prof. E. Armelin, Prof. Dr. C. Alemán
Departament d'Enginyeria Química and Barcelona Research Center in Multiscale Science and Engineering, EEBE, Universitat Politècnica de Catalunya, C/ Eduard Maristany, 10-14, 08019, Barcelona, Spain
E-mail: brenda.guadalupe.molina@upc.edu and carlos.aleman@upc.edu

Dr. J. Casanovas
Departament de Química, Universitat de Lleida, Escola Politècnica Superior, C/ Jaume II nº 69, Lleida E-25001, Spain

Dr. M. M. Pérez-Madrigal, Prof. Dr. C. Alemán
Institute for Bioengineering of Catalonia (IBEC), The Barcelona Institute of Science and Technology, Baldiri Reixac 10-12, 08028 Barcelona Spain

Dr. P. Turon
B. Braun Surgical, S.A.U. Carretera de Terrassa 121, 08191 Rubí (Barcelona), Spain

Keywords: bacteria respiration, bacteria sensors, biomedical implants, flexible sensors, poly(3,4-ethylenedioxythiophene)

Abstract. Rapid detection of bacterial presence on implantable medical devices is essential to prevent biofilm formation, which consists of densely packed bacteria colonies able to withstand antibiotic-mediated killing. In this work, we present a smart approach to integrate electrochemical sensors for detecting bacterial infections in biomedical implants made of isotactic polypropylene (i-PP) using chemical assembly. The electrochemical detection is based on the capacity of conducting polymers (CPs) to detect extracellular nicotinamide adenine dinucleotide (NADH) released from cellular respiration of bacteria, which allows distinguishing prokaryotic from eukaryotic cells. Oxygen plasma functionalized free-standing i-PP, coated with a layer (~1.1 μm in thickness) of CP nanoparticles obtained by oxidative

polymerization, has been used as working electrode for the anodic polymerization of a second CP layer (~8.2 μm in thickness), which provides very high electrochemical activity and stability. The resulting layered material, i-PP_f/CP^2, detects the electro-oxidation of NADH in physiological media with a sensitivity 417 μA/cm^2 and a detection limit up to 0.14 mM, which is below the concentration of extracellular NADH found for bacterial cultures of biofilm-positive and biofilm-negative strains.

1. Introduction

Rapid detection of bacterial pathogens is essential for an effective pathogen-oriented clinical treatment of the infection. At present time, this is particularly important when an improper use of antibacterial agents has accelerated the microbial resistance to antibiotics.[1] The most classical technique for such microbial detection, which consists on bacteria culturing on contact agar plates, takes at least 24 h, requires expertise, and ignores bacteria in the viable non-culturable state (*i.e.* bacteria that fail to grow on media that they would normally grow and develop into a colony capable of metabolic activity).[2]

Within this context, prosthetic infection deserves special mention since it is a tremendous burden for individual patients as well as the global healthcare system. Prostheses provide pain relief, restore function and independence and improve patient quality of life. Moreover, the incidence of prosthesis implantation is expected to continue to rise (*e.g.* in United States alone, the number of knee arthroplasties is expected to increase from 719,000 in 2010 to 3.48 million by 2030[3]). Moreover, the pathogenesis of prosthetic infections is associated with the ability of microorganisms to form biofilms, which are comprised of bacteria and the proteoglycan extracellular matrix they secrete.[4] This matrix protects bacteria from antibiotics and the host immune response, and biofilm is frequently related with the underlying reason for persistence of infections.[4]

Electrochemical sensors can be used to detect bacterial infection in prosthetic devices if several requirements are met.[5,6] The three most important demands to achieve a successful response are: 1) the two elements, the sensor and the prosthetic device, must be properly integrated; 2) the sensor cannot alter the biocompatibility of the materials used to fabricate the prosthetic device; and 3) appropriated bacteria markers must be identified (*i.e.* chemicals with redox properties). On the other hand, even though biofilms can be detected with polymeric sensors using electrochemical impedance spectroscopy (*i.e.* measuring the electrochemical impedance across the electrode-electrolyte interface over a wide range of frequencies),[5,7] the utilization of more simple electrochemical methodologies (*e.g.* voltammetric and potentiometric measures) is highly desirable to facilitate such process.

In recent times, within the focus of biomedical applications, some relevant contributions to the utilization of sensors for the detection of bacterial growth using non-impedance techniques have been published.[8-14] Cernat *et al.*[8] reported a nanohybrid sensor applicable to human serum, saliva and tap water made of graphene, polypyrrole and gold using pyoverdine as chemical marker, the siderophore of *Pseudonomas aeruginosa* (*P. aeruginosa*). More recently, Khalifa *et al.*[9] utilized a polyaniline / gold nanoparticles modified indium tin oxide (ITO) electrode to detect pyocyanin in *P. aeruginosa* infections, using samples collected from patients suffering from corneal ulcers. Simoska *et al.*[10] detected pyocyanin, 5-methylphenazine-1-carboxylic acid and 1-hydroxyphenazine to identify polymicrobial infections from *P. aeruginosa* in different growth media, using transparent carbon ultramicroelectrode arrays. On the other hand, Compton and co-workers[11] showed the selective immobilization of *Escherichia coli* (*E. coli*) and *Neisseria gonorrheae* to gold electrodes, allowing sensitive quantification of expressed cytochrome c oxidase activity in solution. Grauby-Heywang and co-workers[12] engineered a sensor by functionalizing silica nanoparticles with specific polyclonal antibodies for the specific detection of *E. coli*. Tzanov and co-workers[13] developed a smart electrochemical set up assembling a nanoporous

alumina membrane and electrodes made of ITO/poly(ethylene terephthalate), which was used to detect virulence markers, as bacterial hyaluronidase.

In a very recent study, we proposed an electrochemical sensor for bacterial metabolism using the oxidation of nicotinamide adenine dinucleotide (NADH) to detect the growth of Gram-positive and Gram-negative bacteria.[14] The sensor was based on a composite of isotactic polypropylene (i-PP), which is a plastic commonly employed to manufacture medical implants (*i.e.* surgical meshes for hernia repair and sutures), and poly(3,4-ethylenedioxythiophene) nanoparticles (PEDOT NPs), which were incorporated to i-PP films by mechanical pressing. It is worth noting that PEDOT, which is an electroactive and biocompatible conducting polymer (CP),[15] is able to detect the oxidation of NADH at around 0.5-0.7 V.[14,16]

Despite NADH and its oxidized form (NAD+) are involved in the energy metabolism of living cells[17] and in many pathologies (*e.g.* cancer and epilepsy),[18] this marker was never used before to distinguish bacterial proliferation from eukaryotic cells growth.[14] Our approach was based on the fact that aerobic respiration reactions in eukaryotic cells occur in the mitochondria, whose double membrane is impermeable to NADH and NAD+.[19] Therefore, the NADH level in eukaryotic level is restricted to the cytosolic pool. Instead, the respiration of bacteria occurs in the cytosol or on the inner surfaces of the cell membrane, which is permeable to NADH and NAD+ and allows their migration to the extracellular space.[20] This inspired us to use the oxidation of extracellular NADH to NAD+ as target for the detection of bacterial growth without interference coming from the proliferation of eukaryotic cells.[14]

In this work we present a smart approach to integrate PEDOT-based electrochemical sensors for detecting bacterial infection on i-PP implants by chemical assembly. This new strategy, which consists on one functionalization and two different polymerization steps (**Figure 1a**) provides important advantages with respect to the simple mechanical pressing used in

previous works to prepare i-PP/PEDOT NPs composites.[14] After evaluating the chemical, morphological, and electrochemical properties of the new platform, its ability to detect the oxidation of NADH has been carefully examined and demonstrated. A specific focus was to asses that the concentration of extracellular NADH associated to aerobic bacterial metabolism is within the linear range identified for the developed platform and above the limit of detection.

2. Results and Discussion

2.1. Construction of the Sensor: Chemical Assembly of CPs on Functionalized i-PP

A sketch of the three steps used to prepare the sensor integrated in an i-PP film typically used for biomedical implants, which was kindly supplied by Braun Surgical S.A.U. (Rubí, Barcelona, Spain), is shown in Figure 1a. The surface of the i-PP films (6 × 5 cm^2) was functionalized with low pressure radio-frequency (RF) oxygen plasma using the conditions described in the Methods section (ESI). After plasma treatment, which took 180 s, functionalized films were stored under vacuum.

Functionalized i-PP films (i-PP_f) were cut in 0.5 × 1.5 cm^2 samples and a first layer of CP was adhered onto it by chemical oxidative polymerization. For this purpose, the i-PP_f sample was immersed in 5 mL of 0.2 M HCl with 50 mM hydroxymethyl-3,4-ethylenedioxythiophene (MHeDOT) monomer, which is 3,4-ethylenedioxythiophene derivative bearing a hydroxymethyl group to improve the solubility in water,[21] under stirring during 30 min. Then, 1 mL of 0.2 M HCl with 60 mM of ammonium persulfate (APS) was slowly dropped to the solution containing the monomer on i-PP_f. The reaction, with a monomer : oxidant ratio of 1 : 1.2, was kept at 37 °C and 80 rpm. After 24 h, the resulting material, named i-PP_f/CP, was removed, washed with milli-Q water (three times) and acetone (one time), and dried.

Finally, in the third step, a second CP layer was added to the i-PP_f/CP sample. For this purpose, a i-PP_f/CP film, which was used as working electrode, was introduced in a three-electrode cell filled with 20 mL of an acetonitrile solution with 10 mM 3,4-ethylenedioxythiophene (EDOT) monomer and 0.1 M $LiClO_4$ as supporting electrolyte. A PEDOT layer was formed onto the poly(hydroxymethyl-3,4-ethylenedioxythiophene) (PHMeDOT) one by applying a constant potential of +1.40 V and adjusting the polymerization charge to 1.0 C. The aspect of the resulting electroactive i-PP film, hereafter named i-PP_f/CP^2 is compared in Figure 1b with those of i-PP, i-PP_f and i-PP_f/CP. As is shown, the translucent aspect of pristine i-PP changes to whitish (i-PP_f), blueish (i-PP_f/CP) and dark blue (i-PP_f/CP^2), suggesting the success of the steps associated to the plasma functionalization, the integration of the PHMeDOT layer by oxidative polymerization, and the incorporation of the external PEDOT layer by anodic polymerization, respectively. On the other hand, Table 1 summarizes the main differences between the i-PP/CP^2 sensor and that previously reported.[14

2.2. Chemical C**haracterization**

The effects of the plasma functionalization and the successful incorporation of PHMeDOT (1^{st}) and PEDOT (2^{nd}) layers on i-PP_f were investigated using UV-Vis, FTIR and Raman spectroscopies. The UV-Vis spectra recorded for i-PP, i-PP_f, i-PP_f/CP and i-PP_f/CP^2 are compared in **Figure 2a**. As it was expected, no absorption band was detected by UV-Vis spectroscopy for i-PP and i-PP_f. For i-PP_f/CP, the absorption in the range of 300-400 nm decreased due to the n-π electronic transition of aromatic rings, which is typically observed at ~250 nm, while that in the range of 400-750 nm increased, as corresponds to the polaron absorption of the doped PHMeDOT layer.[22] This effect becomes more pronounced for i-PP_f/CP^2, suggesting that the doping level by the electrochemically polymerized PEDOT layer is higher than that of the internal PHMeDOT layer.

The FTIR spectrum of i-PP (Figure 2b) shows the characteristic absorption peaks with the broad and intense bands associated to the C–H stretch vibrations (*ca.* 2920 cm^{-1}), the moderate absorption peaks associated to deformation vibration of the CH_2 group (1455 cm^{-1}), the methyl group vibrations (1376 cm^{-1}), and the characteristic vibration of unsaturated CH_2 groups (841, 999 and 1167 cm^{-1}).[23] The FTIR spectrum of i-PP_f (Figure 2b) reveals new signals appearing at 1534 and 1686 cm^{-1}, which are attributed to C=O stretching, and a band at 1088 cm^{-1} associated to C–O stretching. Detailed discussion of i-PP_f spectrum was reported in a recent work.[24] The presence of PHMeDOT and PEDOT is proved in the spectra of i-PP_f/CP and i-PP_f/CP^2 (Figure 2b) by the characteristic bands of the C–S and C–S–C vibrations in the thiophene ring (869, 757 and 614 cm^{-1}). However, many fingerprints of the CPs are hidden by the predominant bands of i-PP, which is the main component of the composite. To overcome this issue and better visualize the presence of PHMeDOT and PEDOT, the Raman spectra of i-PP, i-PP_f, i-PP_f/CP and i-PP_f/CP^2 were recorded (Figures 2c-d).

Raman spectra of i-PP and i-PP_f, which are compared in Figure 2c, show that the peaks associated to crystalline i-PP (809 and 973 cm^{-1}) become enhanced after plasma treatment.[24] In addition, plasma treatment induces a change in the shape and intensity of the band at 2962 cm^{-1}, which corresponds to the C–H stretching vibrations from methyl groups,[25] as well as a reduction of the CH_3 rocking band at 841 cm^{-1}. These features suggest that the CH_3 groups are modified by the plasma, becoming the favorite site for the formation of oxidized groups, which is in agreement with previous work.[24]

Figure 2d, which compares the Raman spectra of i-PP_f/CP and i-PP_f/CP^2, shows the predominance of CPs bands with respect to the i-PP and i-PP_f ones. This has been attributed to the resonance Raman effect that increases the intensity of the bands of the material when the laser energy coincides with the frequency of the electronic transition of the sample.[26] However, the i-PP_f band at 2962 cm^{-1} is still detectable after the incorporation of the

PHMeDOT layer, whilst it completely disappears after the anodic polymerization of PEDOT. This feature suggests that the thickness of second CP layer in i-PP/$_f$CP^2 is much higher than the PHMeDOT one in i-PP$_f$/CP, as confirmed by profilometry measurements (see below). Furthermore, the spectra reported in Figure 2d exhibit the main characteristics peaks of PHMeDOT and PEDOT: C=C symmetrical stretching (1430 and 1420 cm^{-1}, respectively) and C=C asymmetrical stretching (1500 cm^{-1}).

2.3. Surface characterization

Identification of PHMeDOT and PEDOT at the surface of i-PP$_f$/CP and i-PP$_f$/CP^2 platforms was unambiguously confirmed using X-ray photoelectron spectroscopy (XPS). In a recent investigation, the functional groups created by plasma functionalization were extensively discussed by comparing the XPS spectra of i-PP and i-PP$_f$.[24] **Figure 3a-b** compare the XPS spectra recorded for i-PP$_f$/CP and i-PP$_f$/CP^2. As it was expected, the most intense peaks in both spectra correspond to the C 1s and O 1s. Also, the S 2s and S 2p signals are clearly identified in the two platforms, their intensity being weaker for i-PP$_f$/CP than for i-PP$_f$/CP^2.

Figure 3 includes the high-resolution XPS spectra in the C 1s and O 1s regions for the two platforms. Deconvolution of the C 1s peak led to five and four Gaussian curves for i-PP$_f$/CP and i-PP$_f$/CP^2, respectively. The two systems show the fingerprints of the expected C–C (284.9 eV), C–O (286.0 eV), C–S (287.5 eV) and C=O (289.1) bonds, which come from the i-PP$_f$ substrate and/or the CP chains (PHMeDOT and PEDOT). In addition, i-PP$_f$/CP shows a band at 290.2 eV (Figure 3a), which may be attributed to an undesired reaction between the plasma activated surface and HMeDOT monomer. This band disappears or become inappreciable for i-PP$_f$/CP^2 (Figure 3b) since the signals of anodically polymerized PEDOT predominate over those of PHMeDOT. The high resolution O 1s spectra show Gaussian peaks centered at 530.1 and 532.3 eV, which are associated to C=O and C–O bonds, respectively, and at 534.1 eV. The latter corresponds to the O=C–O fingerprint of the plasma activated i-

PP_f substrate, as was recently proved.[24] The intensity of the latter peak, which is the highest for i-PP_f/CP (Figure 3a), decreases considerably after the incorporation of the PEDOT coating, becoming the weakest for i-PP_f/CP^2 (Figure 3b).

Representative scanning electron microscopy (SEM) micrographs and 3D atomic force microscopy (AFM) images of i-PP, i-PP_f, i-PP_f/CP and i-PP_f/CP^2 are shown in **Figure 4**. The i-PP surface film shows a flat and smooth morphology (Figure 4a), which is modified after exposure to the oxygen plasma. Thus, i-PP_f exhibits a nano-patterning that extends along the whole surface (Figure 4b). This morphological change affects significantly the topography increasing the surface roughness (R_q), as is evidenced by comparing the 3D height AFM images of i-PP and i-PP_f (R_q = 27 ± 5 and 41 ± 7 nm, respectively).

The morphologies of PHMeDOT in i-PP_f/CP are shown in Figure 4c. SEM micrographs evidence that the oxidative polymerization of HMeDOT resulted in the formation of abundant and irregular PHMeDOT NPs between 60 and 200 nm in size (average: 117 ± 38 nm). These NPs are randomly distributed forming a layer of *ca.* 1 μm in thickness, leaving empty spaces among them. The lack of a continuous contact among them affects the formation of conduction paths and explains the poor electrochemical activity of i-PP_f/CP (see below). Besides, the oxidative polymerization step affects the surface topography of i-PP_f, which becomes much more abrupt (R_q = 334 ± 19 nm).

Finally, PHMeDOT NPs were used as polymerization nuclei of PEDOT chains, which were electrochemically generated at a constant potential of +1.40 V. The morphology and topography of i-PP_f/CP^2 (Figure 4d) are very similar to those reported for PEDOT films.[27,28] Thus, anodically polymerized PEDOT organizes in clusters of aggregated molecules that are located at different levels. The roughness, R_q= 603 ± 36 nm, is almost twice the i-PP_f/CP, indicating that PEDOT chains grow not only filling the empty spaces among neighboring PHMeDOT NPs (Figure 4c) but also on the top of the layer. Indeed, PEDOT completely

covers the PHMeDOT NPs, integrating them into a single conducting layer with continuous and well-defined conduction paths. The heterogeneous and porous topography of i-PP_f/CP^2, which is clearly reflected in the 3D height AFM image (Figure 4d), practically matches the organization found for PEDOT films.[28,29] Consistently, the thickness of the conducting layer increases from *ca.* 1 μm for i-PP_f/CP to *ca.* 8 μm for i-PP_f/CP^2.

Finally, the wettability of i-PP, i-PP_f, i-PP_f/CP and i-PP_f/CP^2 was determined by measuring the water contact angle (WCA). The obtained WCA values, which were 102º ± 4º, 78º ± 5º, 81º ± 3º and < 20º, respectively, reflect as expected, the greatest change is produced after the incorporation of the PEDOT layer (Figure S1). Thus, although both the plasma treatment and the incorporation PHMeDOT NPs reduce the hydrophobicity of i-PP, hence, a completely hydrophilic platform is only achieved after coating the i-PP_f/CP with PEDOT.

2.4. Electrochemical characterization

The electrochemical activity of the systems under study was investigated by cyclic voltammetry (CV) using phosphate buffer saline (PBS) solution, pH 7.4, as supporting electrolyte. Control voltammograms recorded for i-PP, i-PP_f and i-PP_f/CP in PBS are compared in **Figure 5a**. As expected, no electrochemical activity was detected for i-PP and i-PP_f (*i.e.* the areas of the voltammograms are negligible). However, the formation of PHMeDOT NPs on the surface of i-PP_f results in an increment of electroactivity, even though the voltammograms recorded for i-PP_f/CP do not show clear oxidation nor reduction processes. This observation, which is consistent with the poor contact the CP NPs (Figure 4c), indicates that formation of redox species in the potential range from −0.20 to +0.80 V is blocked by the i-PP_f matrix.

The incorporation of a PEDOT layer, using the PHMeDOT NPs as polymerization nuclei, results in a huge increase of the electrochemical activity. The transformation associated to the formation of a dense and compact network of PEDOT chains filling the spaces between the

NPs and coating them, as observed by SEM (Figure 4d), is visually detected when the film progressively changes from blueish to dark blue with increasing polymerization charge (Figure 5b). Inspection to the control voltammograms displayed in Figure 5c shows that electroactivity of i-PP$_f$/CP^2 is higher than that of i-PP$_f$/CP by several orders of magnitude. More specifically, the voltammetric charge (Q) and the current density at the reversal potential ($j_{0.8}$) determined for i-PP$_f$/CP are Q= 1.3×10^{-5} C and $j_{0.8}$= 3×10^{-3} mA/cm^2, these parameters increasing to Q= 0.020 C and $j_{0.8}$= 3.28 mA/cm^{-2} for i-PP$_f$/CP^2. This observation confirms that i-PP$_f$/CP^2 can be described as a network of PEDOT-based conduction paths coating the plasma treated i-PP film.

On the other hand, i-PP$_f$/CP^2 exhibits a very high electrochemical stability in PBS. Figure 5c compares the first control voltammogram with that recorded after 50 consecutive oxidation-reduction cycles in the potential range from −0.20 to +0.80 V, both showing very similar anodic and cathodic areas. Indeed, the electrochemical activity of i-PP$_f$/CP^2 decreases by only 1.1% after 50 cycles. This is a very interesting observation since the electrochemical stability of PEDOT in PBS is known to be relatively poor when the scanned potential interval is slightly wider than that used in this work. For example, the electrochemical activity of PEDOT films was reported to decrease by 17% and 39% when 10 and 50 redox cycles were applied in PBS using a potential range from −0.40 to 0.90 V.[30] This is consistent with the fact that the anodic limit for PEDOT polarization occurs at +0.80 V, as reported by Marzocchi *et al.*,[31] while higher potential values lead to a strong overoxidation of the CP.

2.5. Electrochemical detection of NADH

Before to examine the detection of NADH using the i-PP$_f$/CP^2 platform, in this section we investigate an interesting point that deserves consideration. This is the effect of the CP on the chemistry of the NAD+/NADH redox pair, which we have studied using theoretical methods based on Density Functional Theory (DFT) calculations at the B3LYP/6-31+G(d,p) level. The

processes involved in the electrochemical reduction of NADH and the electrochemical oxidation of its reduced form NAD+ are displayed in Scheme 1. Although previous studies suggested that the nicotinamide moiety is responsible of the NAD+/NADH redox,[32] calculations displayed in this section were conducted considering the whole real molecule.

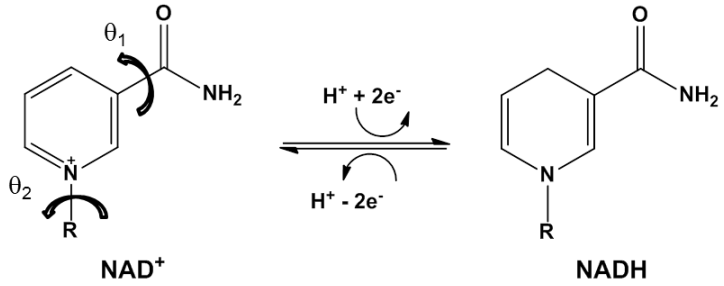

Scheme 1. Electrochemical reaction of the NAD+/NADH redox pair.

The thermodynamic cycle displayed in **Figure 6a** has been used to estimate the oxidation potential of NADH to NAD+ referred to the standard hydrogen electrode. For this purpose, the four structures of lower energy found in the conformational sampling reported by Cao *et al.*[33] for NADH and NAD+ were used as starting points. For each of these structures, the dihedral angles θ_1 and θ_2 (see Scheme 1) were systematically varied between 0º and 360º in steps of 60º. All these structures were optimized in the gas-phase. In order to calculate the Gibbs free energy in the gas-phase, $\Delta G^0(gp)$, frequency calculations were performed for the five conformations of lowest energy. Such five structures were re-optimized in aqueous solution by applying the SMD universal solvation model developed by Truhlar and co-workers[34] within the B3LYP/6-31+G(d,p) framework. The SMD model calculates the solvation free energy, ΔG_{sol}, as the sum of two contributions. The first contribution arises from a self-consistent reaction field treatment that involves the solution of the non-homogeneous Poisson equation for electrostatic component in terms of the integral equation-formalism polarizable continuum model (IEF-PCM). The second contribution, which represents short-range interactions between the solute and solvent molecules in the first

solvation shell, is a sum of terms that are proportional to the solvent-accessible surface areas of the individual atoms of the solute.

According to the thermodynamic cycle shown in Figure 6a, the free energy associated to the reduction of NAD+ to NADH in aqueous solution at 298 K and 1 atm, $\Delta G^0(aq)$, was calculated as:

$$\Delta G^0(aq) = \Delta G^0(gp) + \Delta G_{sol} - \Delta G_{sol\text{-}Ox} - \Delta G_{sol,H+} \quad (1)$$

where ΔG_{sol} and $\Delta G_{sol\text{-}Ox}$ are the solvation energies of NADH and NAD+, respectively, and $\Delta G_{sol,H+}$ is the solvation energy of the H_3O^+ specie, which was taken from experiments reported in the literature ($\Delta G_{sol,H+}$= -261 kcal/mol).[35] The value of $\Delta G^0(aq)$ was corrected to change from 1atm to a 1 M solution, $\Delta G^0(aq;1M)$, using Eq 2:[36]

$$\Delta G^0(aq;1M) = \Delta G^0(aq) + \Delta n \cdot R \cdot T \cdot \ln(24.46) \quad (2)$$

The value of $\Delta G^0(aq;1M)$ for the lowest energy conformations of NADH and NAD+, which are shown in Figure 6b, was -195.64 kcal/mol. This was transformed into the reduction standard potential, E^0 (Eq 3), and referred to the standard hydrogen electrode (SHE), $E^{0'}$ (Eq 4):

$$\Delta G^0(aq;1M) = -n \cdot F \cdot E^0 \quad (3)$$

$$E^{0'} = E^0 - E_{SHE} \quad (4)$$

where n is the number of involved electrons (n= 2), F is the Faraday constant (23.061 kcal/(mol·V), and E_{SHE} is the reduction potential of the SHE in water, which was taken from the literature (E_{SHE}= 4.44 V).[37]

The $E^{0'}$ predicted from theoretical calculations is –0.20 V, which is in good agreement with experimental redox potential for NAD, which is –0.32 V.[38] However, the utilization of PEDOT-modified electrodes may affect the redox behavior of the NAD+/NADH pair. Thus, the formation of specific interactions between the biomolecule and the PEDOT electrode could affect the electron transfer process altering the position of the oxidation and reduction

peaks or, even, inhibit them. In order to get deeper understanding on this possibility, DFT calculations on NAD+···CP and NADH···CP model complexes were used to evaluate the variation of the $E^{0'}$ with respect to the value found to the isolated molecule. More specifically, calculations were repeated considering the interaction of the analyte with a tetrathiophene oligomer. Geometry optimizations of complexes in the gas-phase and aqueous solution were carried out considering, for NADH and NAD+, the five structures used above for the isolated molecules.

Figure 6c shows the most stable NAD+···CP and NADH···CP complexes, illustrating the interaction between the analyte and the π-system of the tetrathiophene oligomer. The $E^{0'}$ predicted from these DFT calculations is –0.16 V, indicating that the charge transfer between the analyte and π-system of CP produces a small shift towards higher potentials. Obviously, this shift is expected to be higher in real systems because of the bulk electronic effects. Thus, NADH and, especially, charged NAD+ are expected to form more interactions with the π-conjugated chains when a completely coated CP is considered.

2.6. Electrochemical detection of NADH using i-PP_f/CP^2

The electrochemical performance of the free-standing i-PP_f/CP^2 sensor probe towards the electrocatalytic oxidation of NADH was examined by CV in Dulbecco's modified Eagle's medium (DMEM) supplemented with 2% fetal bovine serum (FBS; pH 8.1) and 0.2% $NaHCO_3$. As shown in **Figure 7a and 7b**, which compare the voltammograms recorded for increasing NADH concentrations (*i.e.* from 0 to 2 mM and from 2 to 16 mM, respectively), the oxidation of NADH to NAD+ is evidenced by oxidation peak at around 0.6 V.

The peak potential for NADH electro-oxidation shifted positively at 170 mV when the NADH concentration increased from 0.25 mM to 16 mM (*i.e.* from 0.52 V to 0.69 V), while the peak current density increased 1.88 mA/cm^2 (*i.e.* from 4.17 to 6.05 mA/cm^2). As the amount of analyte···CP interactions increases with the NADH concentration, these shifts are fully

consistent with theoretical predictions and, therefore, the peak cannot be ascribed to any other process different from the oxidation of NADH to NAD+. Furthermore, a change in the slope is observed when peak current density (y; in mA/cm^2) is plotted versus the amount of NADH (x; in mM). More specifically, the linear dynamic interval observed from 0 to 2 mM (Figure 7a, right) with linear regression equation $y= 0.4174 \cdot x + 4.1056$ ($R^2= 0.9559$) changes to $y= 0.0759 \cdot x + 4.9028$ ($R^2= 0.9282$) in the interval from 2 to 16 mM (Figure 7b, right). The slope of the equation corresponds to the linear sensitivity, which is 417 and 75.9 μA/cm^2 for the 0-2 and 2-16 linear dynamic range, respectively.

The limit of detection (LOD) of the i-PP$_f$/CP^2 sensor, which is defined as $(3 \cdot \sigma)/b$, where σ is the standard deviation of the blank and b is the slope of the calibration curve in the lowest dynamic range, is found to be 0.14 mM. This LOD value, which was obtained using self-supported i-PP$_f$/CP^2 films as working electrode, is lower than that reported for electropolymerized PEDOT films supported onto glassy carbon electrodes (LOD= 0.50 mM).[39]

As a first approach, the change in the slope for NADH concentrations higher than 2 mM has been attributed to changes in the aggregation state of NADH molecules. More specifically, NADH has been supposed to be solubilized or forming small molecular cluster for concentrations ≤ 2 mM, whereas NADH aggregates with itself or with other components of the medium for concentrations > 2 mM. This aggregation behavior, which is supposed to increase with the concentration of NADH, would explain the anomalies observed not only in the electrochemical detection but also in the optical one (see below). On the other hand, the response time of the i-PP$_f$/CP^2 sensor was evaluated by CV considering a 10 mM NADH solution in PBS and recording the voltammograms at different the scan rates. Results, which are displayed in Figure S2, indicate that the peak potential for NADH electro-oxidation is detected at all the tested scan rates. In addition, the stability of the i-PP$_f$/CP^2 sensor against the

pH of the medium was demonstrated by recording the voltammograms at pHs ranging between 4 and 8 (Figure S3). The selectivity towards NADH was analyzed using uric acid (UA) and ascorbic acid (AA) as interferents. **Figure 8a** compares the cyclic voltammograms recorded for a 0.1 M PBS (pH 7.4) solution containing10 mM NADH alone or mixed with 10 mM UA and/or 10 mM AA. As it can be seen, the oxidation peak potential is clearly lower for UA and AA than for NADH, the three peaks being well-defined and well-resolved in all cases. Finally, the electrochemical active surface area (ECSA) of the sensor was obtained by CV in 0.1 M PBS (pH 7.4).[40] The scan rate was varied from 10 to 150 mV/s. Figure 8b displays the recorded voltammograms, while Figure 8c plots the change of current density in the potential of +0.8 V ($j_{0.8}$) as function of the scan rate. The slope represents the differential capacitance (C = 0.0275 mF/cm^2). The ECSA of the electrode was estimated by dividing the value of C into Cs, where Cs is the capacitive behavior of the PEDOT. The value of C_S was found from the CV recorded at 50 mV/s (Cs = Q/ΔV = 0.080 mF/cm^2). The resulting ECSA value, 0.343, indicates that 34.3% of the surface area is electroactive.

2.7. Characterizing extracellular NADH from aerobic bacterial metabolism

In this section, we determine the concentration of NADH in extracellular media produced by the aerobic respiration reactions of bacteria. For this purpose, the spectroscopic detection of NADH as a function of its concentration has been studied first. **Figure 9a** (left) shows the UV-Vis spectrum recorded for a 0.25 mM NADH solution in DMEM supplemented with FBS and $NaHCO_3$. Although the most intense peak at 340 nm confirms that NADH is the predominant specie, the presence of the peak at 250 nm evidences the partial oxidation to NAD+ in the used medium. On the other hand, Figure 9a (right) displays the calibration curve obtained using the absorbance at λ= 340 nm for the interval of NADH concentrations from 0 to 2 mM. A linear regression equation, y= 1.5916·x + 0.1883 (R^2= 0.9972), with a LOD of 0.01 mM is obtained for this NADH concentration interval. However, both a drastic change in

the slope and a loss of linearity is observed for the interval of NADH concentrations higher than 2 mM (Figure S4).

These observations, which are fully consistent with the results obtained for the electrochemical detection of NADH in supplemented DMEM using i-PP_f/CP^2 (Figure 7), confirms the difficulty in detecting high concentrations of this analyte. Dynamic light scattering (DLS) measurements provided some light on this feature (Figure S5), suggesting that NADH integrates into protein-forming aggregates, this phenomenon increasing with NADH concentration. Two aggregate distributions in absence of NADH were detected in the DMEM high glucose supplemented with 2% FBS and 0.2% $NaHCO_3$ used in this work (Figure S5a). The first one displays an average size of 19 ± 3 nm, while for the second one is 167 ± 49 nm on average. The size of the aggregates remained approximately unaltered (*i.e.* 17 ± 2 and 177 ± 44 nm, respectively) after the addition of 1 mM NADH (Figure S5b). However, they increased to 22 ± 4 and 265 ± 128 nm when the concentration of NADH was 10 mM (Figure S5c). These features suggest that, although the formation of aggregates is not promoted by NADH, its interaction with the proteins present in the media might lead to slightly bigger particles when the concentration is high enough, which adsorb on the electrode affecting both the electrochemical and spectroscopic detection to a greater extent.

In order to ascertain if the concentration of NADH in media with high contents of bacteria is within the interval of quantification with linear response, *Escherichia coli (E. coli*) colony forming units (CFU, 2×10^8 colony) were seeded in DMEM supplemented with FBS and $NaHCO_3$. The bacteria used for this purpose were ATCC 25922, a biofilm-positive strain (B+), and CECT 101 a biofilm-negative strain (B–). Colonies were incubated at 37 ºC and 80 rpm for 24 h and 48 h maintaining conditions. After such periods of time, the concentrations of NADH in the culture media were determined by measuring the absorbance at λ= 340 nm and applying the calibration curve displayed in **Figure 9a**.

Figure 9b represents the absorbance at λ= 340 nm obtained for B+ and B– cultures after 24 and 48 h (left) as well as the NADH concentrations calculated by applying the corresponding calibration curve (right). The NADH concentration, which was null after seeding the bacteria in the medium, grows with time, independently of the ability to form biofilm. Thus, after 24 h the NADH concentration is 0.25 and 0.34 mM for B+ and B–, respectively, increasing 36% and 8%, respectively, after 48 h. Furthermore, the NADH concentration is higher for B– than for B+. This expected behavior has been attributed to compactness of the biofilm structure, which comprises a self-produced matrix of extracellular polymeric substances and restricts the release of NADH to the medium. Overall, these results confirm that cellular membranes are permeable to NADH produced by bacteria respiration reactions. Moreover, the NADH concentration in the culture media is above the LOD found for i-PP_f/CP^2 and below 2 mM, and, therefore, detectable by both CV and UV-vis spectroscopy.

The bacteria coatings formed on the i-PP_f/CP^2 surface are evidenced in **Figure 10**, which displays representative SEM micrographs. Elemental maps reflect the difference between B+ or B– *E. coli* cells. Thus, after 24 h B+ cells colonize the main part of the surface, forming dense, compact and relatively continuous biofilms. Instead, B– cells only appear colonize small discontinuous zones. **Figure 11** shows the electrochemical detection by CV of NADH coming from bacteria respiration reactions. For this purpose, the same amount (CFU/mL) of B+ or B– *E. coli* cells cultured in DMEM supplemented with FBS and $NaHCO_3$were added to different volumes of fresh supplemented medium (*i.e.* 100, 300 or 500 mL). The controls consisted in 100 mL of DMEM supplemented without bacteria. After 24 h at 37 °C and 80 rpm, the solutions (*i.e*. the controls and the B+ and B– cultures) were centrifuged, and the supernatant was frozen in liquid nitrogen and lyophilized. Then, different aqueous solutions were prepared using the lyophilized bacteria medium. These solutions, which contained different concentration of NADH coming from bacteria metabolism, were used as electrolytic media for CV measurements. The cyclic voltammograms recorded using the different

electrolytic media coming from for B+ and B– cultures, which are shown in Figure 11a-b, allowed us to consider the effect of the bacteria growth cycle in the dynamics of the NADH concentration. In both cases, the current density at the peak potential (zoom images) increases with the concentration of NADH in the medium following the expected linear behavior (Figure 11c-d). For B+ and B– bacteria the concentration of NADH, which was estimated using the recorded voltammograms (Figure 11a-b) and the calibration curves (Figure 7), ranged from 0.01 ± 0.01 to 0.76 ± 0.19 mM and from 0.66 ± 0.11 to 2.32 ± 0.24 mM, respectively.

3. Conclusion

CP-based biosensors for the detection of bacterial infections have been incorporated to free-standing i-PP films for biomedical implants. For this purpose, the following three step approach has been applied: *i)* functionalization of the i-PP surface using an oxygen plasma treatment (i-PP_f); *ii)* deposition on the surface of the plasma treated film of a CP layer (~1.1 μm), which consisted of PHMeDOT NPs prepared by oxidative polymerization (i-PP_f/CP); and *iii)* electrochemical deposition of a PEDOT layer (~8.2 μm) covering the PHMeDOT NPs and filling the spaces among them to improve the electrochemical properties (i-PP_f/CP^2). Indeed, the electrochemical response of i-PP_f/CP^2 is several orders of magnitude higher than that of i-PP_f/CP because of the effective conduction paths formed during the electropolymerization of PEDOT. Although the interaction between the π-system of the CP chains and the NADH affects the position of the oxidation peak of the latter, the i-PP_f/CP^2 platform is able to detect NADH with a linear sensitivity of 417 μA/cm^2. Furthermore, the limit of detection is 0.14 mM, which is below the concentration of extracellular NADH from aerobic bacterial metabolism.

In summary, results indicate that i-PP_f/CP^2 approach is highly promising for bacteria detection on flexible medical implants and rigid prostheses. In future work, this two-layered CP-based

technology will be adapted to i-PP surgical meshes and coupled with plasmonic gold NPs, which efficiently convert near-infrared light into heat to eliminate bacteria.[41] This smart dual system is expected to prevent mesh infections by inhibiting the bacterial growth once detected.

Supporting Information
Supporting Information is available from the Wiley Online Library or from the author.

Acknowledgements

Authors acknowledge MINECO/FEDER (RTI2018-098951-B-I00), the Agència de Gestió d'Ajuts Universitaris i de Recerca (2017SGR359) and B. Braun Surgical, S.A. for financial support. Support for the research of C.A. is grateful to ICREA Academia program for excellence in research.

Received: ((will be filled in by the editorial staff))
Revised: ((will be filled in by the editorial staff))
Published online: ((will be filled in by the editorial staff))

References

[1] M. Mendelson, "Global Governance Must Include the Voices of LMICs to Alter the Tide of Antimicrobial Resistance" in Annual Report of the Chief Medical Officer, Vol. 2, 2019. Infections and the Rise of Antimicrobial Resistance (Ed: S. C. Davies), pp 87-88, London **2019**.

[2] M. Amiri, A. Bezaatpour, H. Jafari, R. Boukhrroub, S. Szunerits, ACS Sens. 2018, 3, 1069.

[3] S. Kurtz, K. Ong, E. Lau, F. Mowat, M. Halpern, J. Bone Joint Surg. Am. 2007, 89,780.

[4] J. W. Costerton, *Science* **1999**, *284*, 1318.

[5] A. L. Furst, M. B. Francis, *Chem. Rev.* **2019**, *119*, 700.

[6] a) M. Amiri, A. Bezaatpour, H. Jafari, R. Boukherroub, S. Szunerits. *ACS Sens.* **2018**, *3*, 1069; b) O. Simoska, K. Stevenson, *Analyst* **2019**, *144*, 6461.

[7] a) L. Y. Zheng, R. B. Congdon, O. A. Sadik, C. N. H. Marques, D. G. Davies, B. G. Sammakia, L. M. Lesperance, J. N. Turner, *Sens. Actuators B* **2013**, *182*, 725; b) A. C. Ward, A. J. Hannah, S. L. Kendrick, N. P. Tucker, G. MacGregor, P. Connolly, *Biosens. Bioelectron.* **2018**, *110*, 65; c) J. B. J. H. van Duuren, M. Müsken, B. Karge, J. Tomasch, C. Wittmann, S. Häussler, M. Brönstrup, *Sci. Rep.* **2017**, *7*, 5223

[8] A. Cernat, M. Tertis, I. Gandouzi, A. Bakhrouf, M. Suciu, C. Cristea, *Electrochem. Commun.* **20185**, *88*, 5.

[9] M. W. Khalifa, A. A. Elkhawaga, M. A. Hassan, A. M. Zahran, A. M. Fathalla, W. A. El-Said, O. El-Badawy, *Sci. Rep.* **2019**, *9*, 18320.

[10] O. Simoska, M. Sans, L. Eberlin, J. B. Shear, K. J. Stevenson, *Biosens. Bioelectron.* **2019**, *142*, 111538.

[11] S. Kus, R. A. S. Couto, R. M. Evans, H. Lavdender, C. C. Tang, R. G. Compton, *Anal. Chem.* **2019**, *91*, 4317.

[12] M. Mathelié-Guinlet, T. Cohen-Bouhacina, I. Gammoudi, A. Martin, L. Béven, M.-H. Grayby-Heywang, *Sens. Actuators B* **2019**, *292*, 314.

[13] A. de la Escosura-Muñiz, K. Ivanova, T. Tzanov, *ACS Appl. Mater. Interfaces* **2019**, *11*, 13140.

[14] B. G. Molina, L. J. del Valle, P. Turon, E. Armelin, C. Alemán, *J. Phys. Chem. C* **2019**, *123*, 22181.

[15] a) L. J. del Valle, F. Estrany, E. Armelin, R. Oliver, C. Alemán, *Macromol. Biosci.* **2008**, *8*, 1144; b) A. Puiggalí-Jou, P. Micheletti, F. Estrany, L. J. del Valle, C. Alemán, *Adv. Healthcare Mater.* **2017**, *6*, 1700453.

[16] a) L. Meng, A. P. F. Turner, W. C. Mak, *Biosens. Bioelectron.* **2018**, *120*, 115; b) C. Sriprachuabwong, C. Karuwan, A. Wisitsorrat, D. Phokharatkul, T. Lomas, P. Sritongkham, A. Tuantranon, *J. Mater. Chem.* **2012**, *22*, 5478.

[17] R. C. Bohinski, In Modern Concepts in Biochemistry; Bacon, Inc.: Newton, MA, **1987**, 567−604.

[18] a) Q. Zhang, S. Y. Wang, A. C. Nottke, J. V. Rocheleau, D. W. Piston, R. H. Goodman, *Proc. Natl. Acad. Sci. U.S.A.* **2006**, *103*, 9029; b) M. Garriga-Canut, B. Schoenike, R. Qazi, K. Bergendah, T. J. Daley, R. M. Pfender, J. F. Morrison, J. Ockuly, C. Satstrom, T. Sutula, *Nat. Neurosci.* **2006**, *9*, 1382.

[19] a) M. Pittelli, L. Formentini, G. Faraco, A. Lapucci, E. Rapizzi, F. Cialdai, G. Romano, G. Moneti, F. Moroni, A. Chiarugi, *J. Biol. Chem.* **2010**, *285*, 34106; b) M. Barile, S. Passarella, G., Danese, E. Quagliariello, *Mol. Biol. Int.* **1196**, *38*, 297; c) L. R. Stein, S.-i. Imai, *Trends Endocrinol. Metab.* **2012**, 23, 420.

[20] Y. Liu, R. Landick, S. Raman, *ACS Synth. Biol.* **2019**, *8*, 264.

[21] G. Fabregat, J. Casanovas, E. Redondo, E. Armelin, C. Alemán, *Phys. Chem. Chem. Phys.* **2014**, *16*. 7850.

[22] S. Garreau, G. Louarn, J. P. Buisson, G. Froyer, S. Lefrant, *Macromolecules* **1999**, *32*, 6807.

[23] B. H. Stuart, *Infrared Spectroscopy: Fundamentals and Aplications*, John Wiley & Sons, New York, NY, USA, 2002.

[24] a) S. Lanzalaco, P. Turon, C. Weis, C. Alemán, E. Armelin, *Soft Matter* **2019**, *15*, 3432; b) S. Lanzalaco, L. J. del Valle, P. Turon, C. Weis, F. Estrany, C. Alemán, E. Armelin, *J. Mater. Chem. B* **2020**, *8*, 1049.

[25] M. Arruebarrena de Baez, P. J. Hendra, M. Judkins, *Spectrochim. Acta, Part A* **1995**, *51*, 2117.

[26] a) A. Shakoor, T. Z. Rizvi, *J. Raman Spectrosc.* **2010**, *41*, 237; b) R. V. Salvatierra, L. G. Moura, M. M. Oliveira, M. A. Pimienta, A. J. G. Zarbin, *J. Raman Spectrosc.* **2012**, *43*, 1094−1100.

[27] D. Aradilla, F. Estrany, C. Alemán, *J. Phys. Chem. C* **2011**, *115*, 8430.

[28] D. Aradilla, D. Azambuja, F. Estrany, M. T. Casas, C. A. Ferreira, C. Alemán, *J. Mater. Chem.* **2012**, *22*, 13110.

[29] C. Ocampo, R. Oliver, E. Armelin, C. Alemán, F. Estrany, *J. Polym. Res.* **2006**, *13*, 193.

[30] a) D. López-Pérez, D. Aradilla, F. Estrany, C. Alemán, *J. Phys. Chem. C* **2013**, *117*, 6607; b) S. Maione, A. M. Gil, G. Fabregat, L. J. del Valle, J. Triguero, A. Laurent, D. Jacquemin, F. Estrany, A. I. Jiménez, D. Zanuy, C. Cativiela, C. Alemán, *Biomater. Sci.* **2015**, *3*, 1395.

[31] M. Marzocchi, I. Gualandi, M. Calienni, I. Zironi, E. Scavetta, G. Castellani, B. Fabroni, *ACS Appl. Mater. Interfaces* **2015**, *7*, 17993.

[32] X. Cao, L. Wu, J. Zhang, M. Dolg, *J. Comput. Chem.* **2020**, *41*, 305.

[33] T. Matsui, Y. Kitagawa, M. Okumura, Y. Shigeta, *J. Phys. Chem. A* 2015, **119**, 369.

[34] A. V. Marenich, C. J. Cramer, D. G. Thuhlar, *J. Phys. Chem. B* **2009**, *113*, 6378.

[35] J. A. Mejias, S. Lago *J. Chem. Phys.* **2000**, *113*, 7306.

[36] C. J. Cramer, Essential of Computational Chemistry Theories and Models, 2nd ed; John Wiley and Sons: Hoboken, NJ, USA; pp.378-379.

[37] S. Trasatti, *Pure Appl. Chem*. **1986**, *58*, 955.

[38] D. F. Wilson, M. Erecinska, P. L. Dutton, *Annu. Rev. Biophys. Bioeng.* **1974**, *3*, 203.

[39] V. S. Vasantha, S.-M. Chen, *Electrochim. Acta* **2006**, *52*, 665.

[40] a) S. Trassatti, O. A. Petrii, *J. Electroanal. Chem.* **1992**, *327*, 353; b) A. García-Miranda Ferrari, C. W. Foster, P. J. Kelly, D. A. C. Brownson, C. E. Banks, *Biosensors* **2018**, *8*, 53.

[41] I. de Miguel, I. Prieto, A. Albornoz, V. Sanz, C. Weis, P. Turon, R. Quidant, *Nano Lett.* **2019**, *19*, 2524.

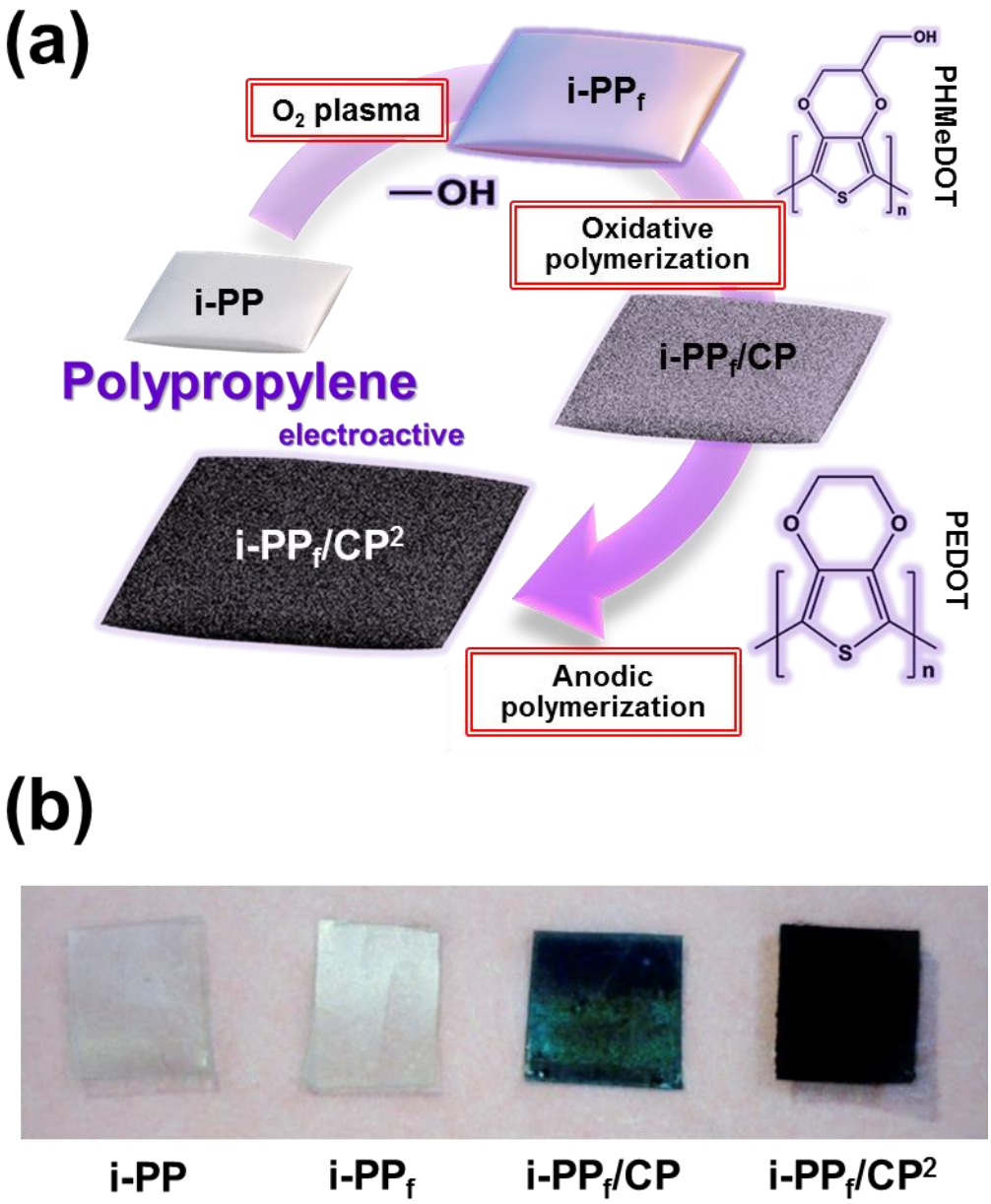

Figure 1. (a) Sketch representing the three steps used to transform i-PP into i-PPf/CP^2, and electroactive i-PP with sensing properties. (b) Photographs of pristine i-PP, i-PP_f, i-PP_f/CP and i-PP_f/CP^2 films.

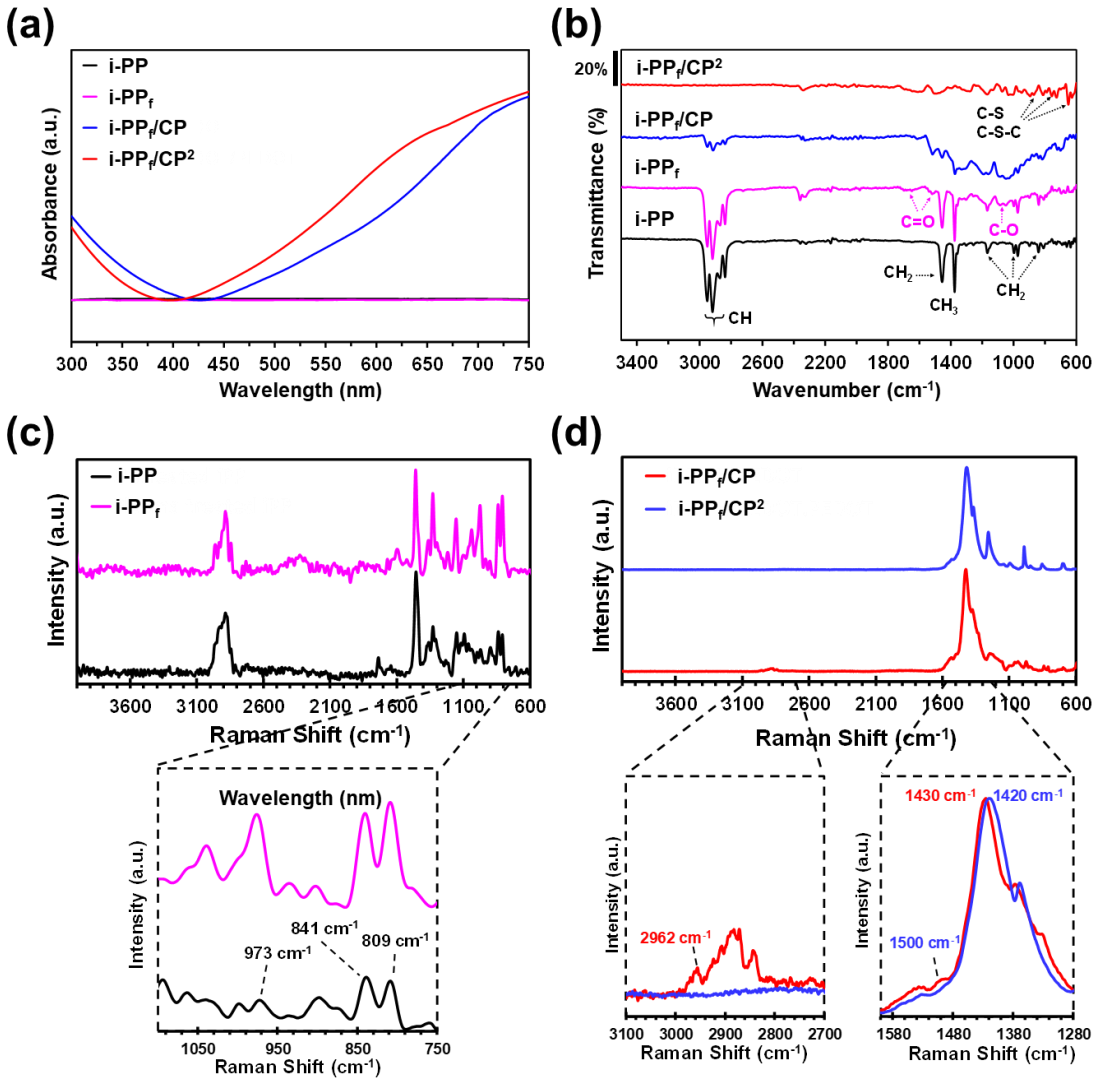

Figure 2. (a) UV-Vis, (b) FTIR and (c, d) micro-Raman spectra i-PP, i-PP$_f$, i-PP$_f$/CP and i-PP$_f$/CP^2.

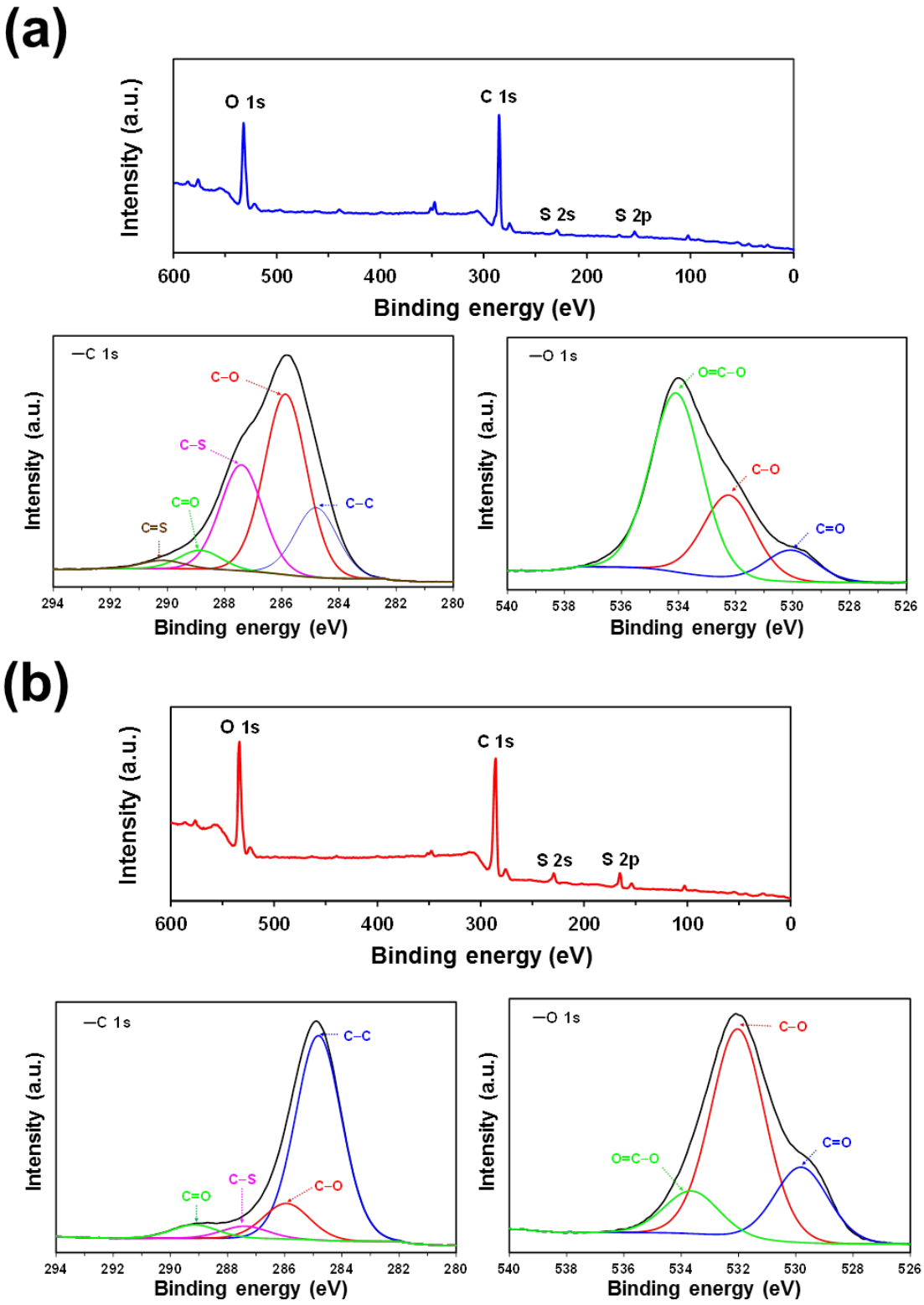

Figure 3. XPS survey spectra (top) and high resolution XPS spectra of C 1s and O 1s elements (bottom left and right, respectively) for (a) i-PP_f/CP and (b) i-PP_f/CP^2.

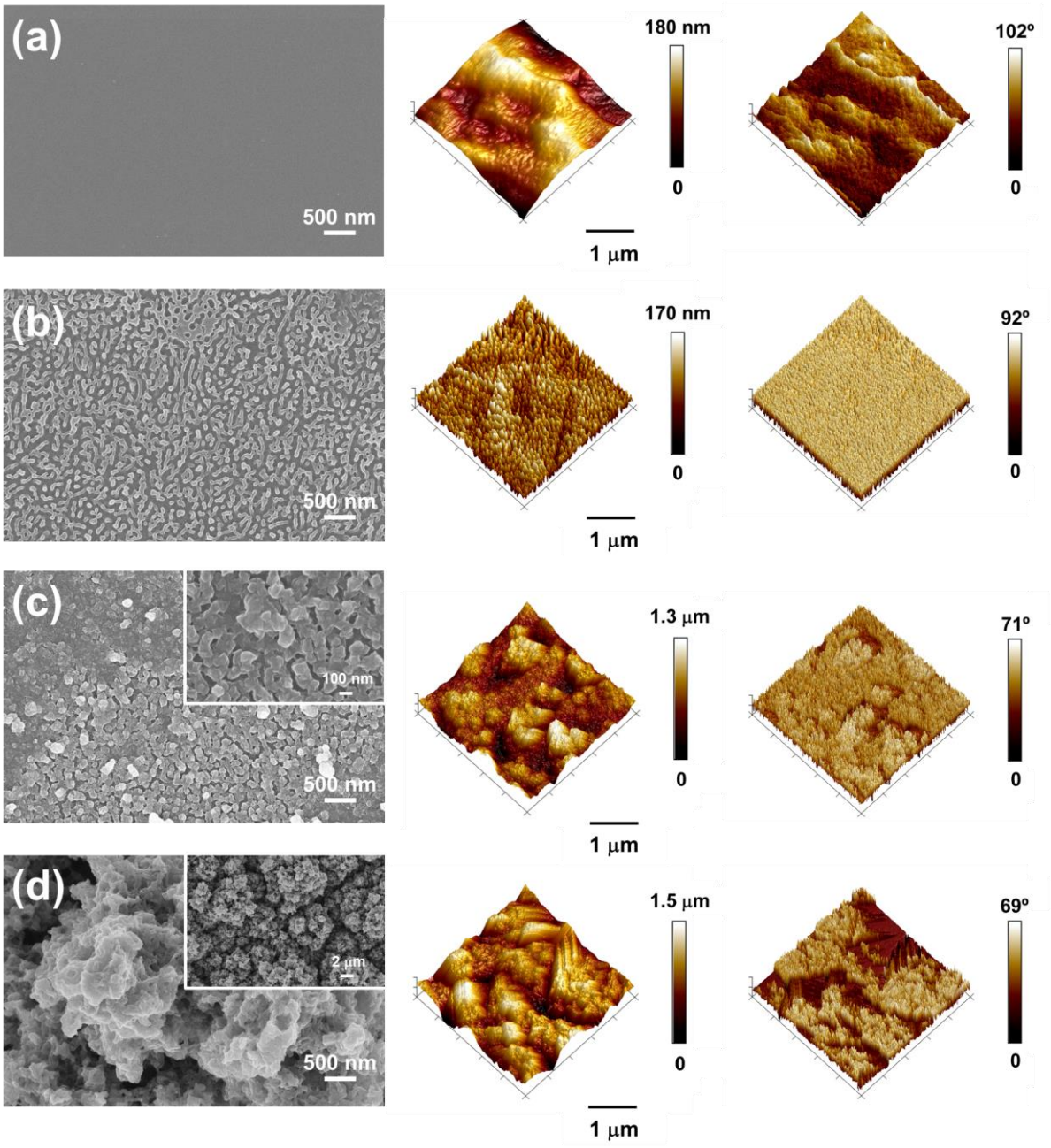

Figure 4. Representative high resolution SEM micrograph (left) and both 3D height and phase AFM images (center and right, respectively) of (a) i-PP, (b) i-PP_f, (c) i-PP_f/CP and (d) i-PP_f/CP^2.

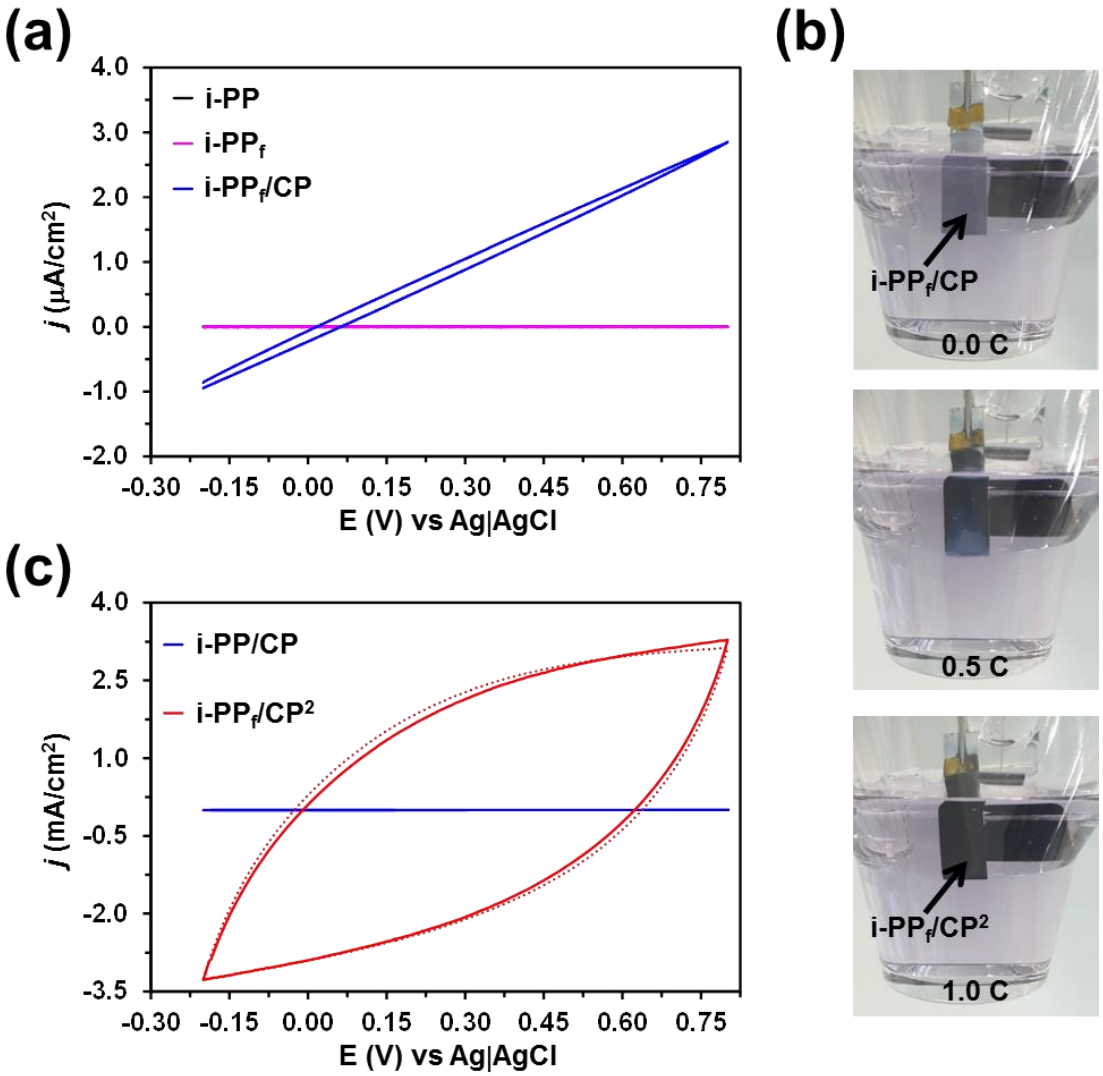

Figure 5. (a) Control voltammograms of i-PP, i-PP$_f$ and i-PP$_f$/CP in PBS. (b) Photographs displaying the progressive variation of the color when i-PP$_f$/CP transforms into i-PP$_f$/CP^2 by polymerizing the upper PEDOT layer. (c) Control voltammograms of i-PP$_f$/CP and i-PP$_f$/CP^2 in PBS. The voltammogram recorded for i-PP$_f$/CP^2 after 50 consecutive oxidation-reduction cycles is also displayed (dotted red curve). For (a) and (c): initial and final potentials, −0.20 V; reversal potential, +0.80 V; scan rate: 50 mV/s.

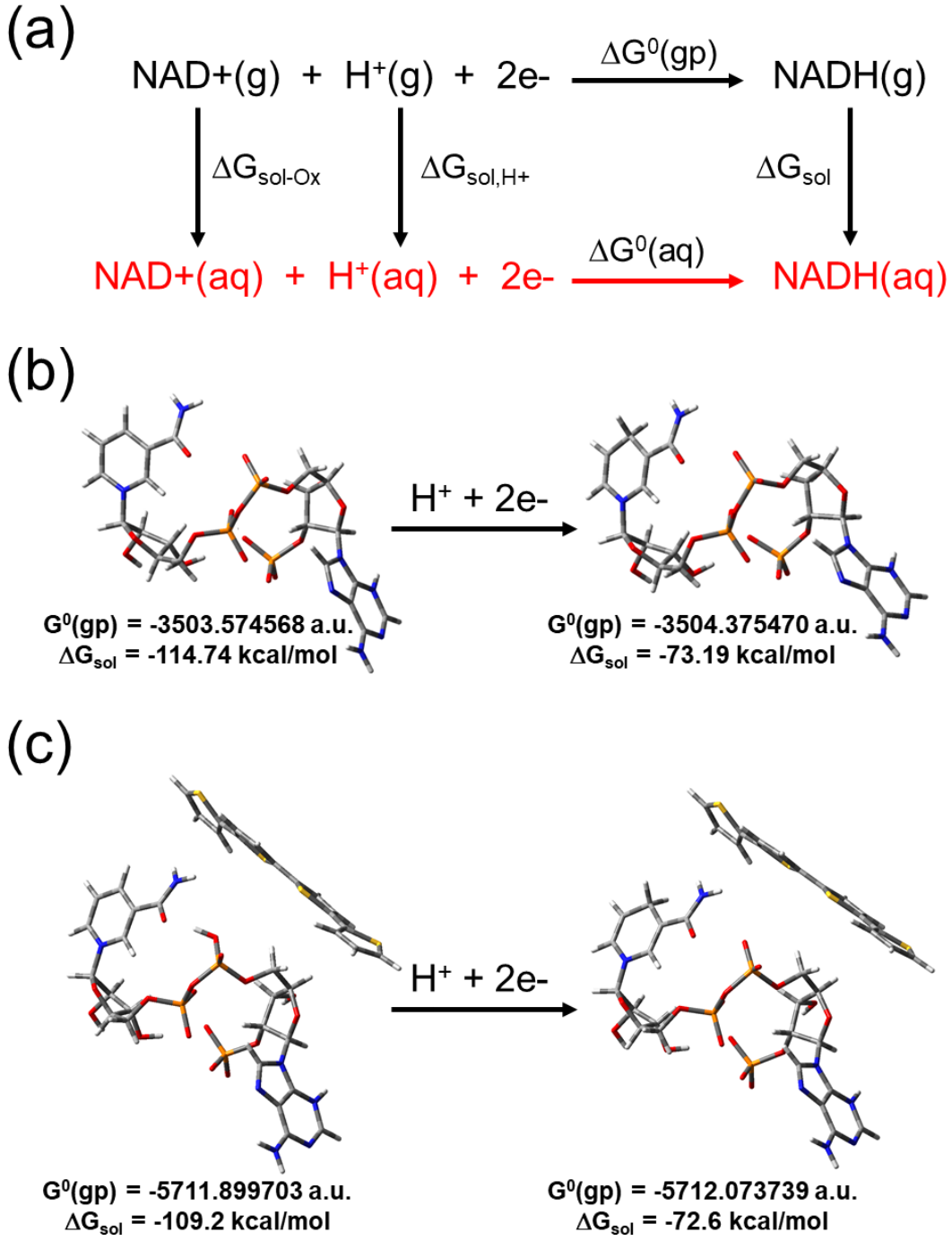

Figure 6. (a) Themodynamic cycle used to predict the free energy associated to the reduction of NAD+ to NADH in aqueous solution at 298 K and 1 atm, ΔG^0(aq). Minimum energy structure calculated for (b) NAD+ and NADH in aqueous solution and (c) NAD+···CP and NADH···CP in aqueous solution. Calculations were performed using the SMD model at the B3LYP/6-31+G(d,p) level.

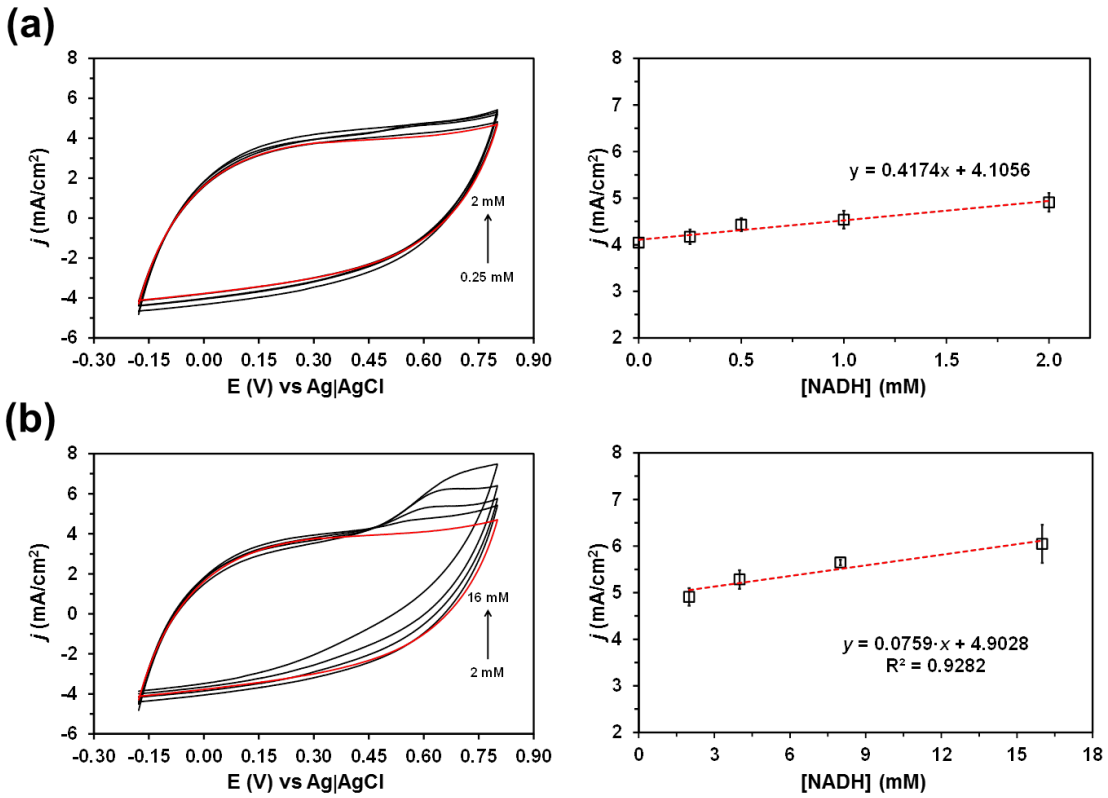

Figure 7. Control voltammograms (left) for i-PP_f/CP^2 of DMEM solutions with NADH concentrations from (a) 0.25 to 2 mM and (b) from 2 to 16 mM. The corresponding calibration curves (*i.e.* peak current *vs.* NADH concentration) are also depicted (right). The red curves correspond to the blanks (*i.e.* DMEM solutions without NADH).

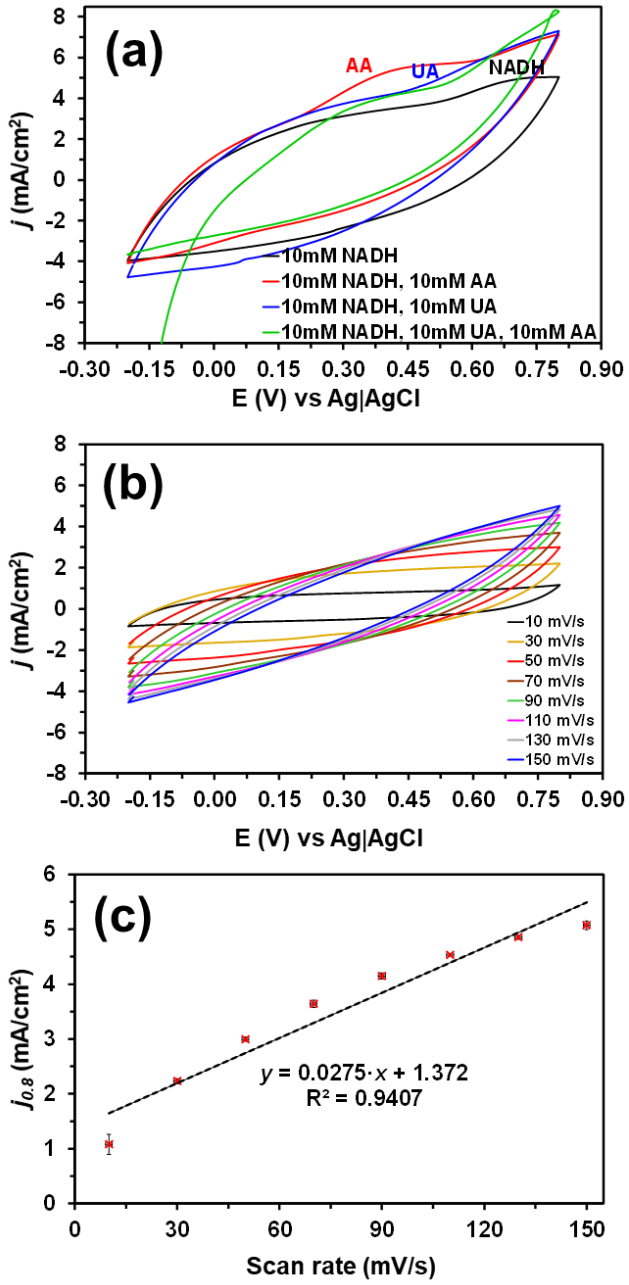

Figure 8. Control voltammograms for i-PP_f/CP^2 in: (a) 0.1 M PBS (pH 7.4) containing 10 mM NADH alone or mixed 10 mM UA and/or 10 mM AA. Scan rate: 50 mV/s; and (b) 0.1 M PBS (pH 7.4) at different scan rates. Initial and final potentials: -0.20 V; reversal potential: +0.80 V. (c) Variation of the current density in the potential of +0.8 V ($j_{0.8}$) as function of the scan rate (taken from graphic b).

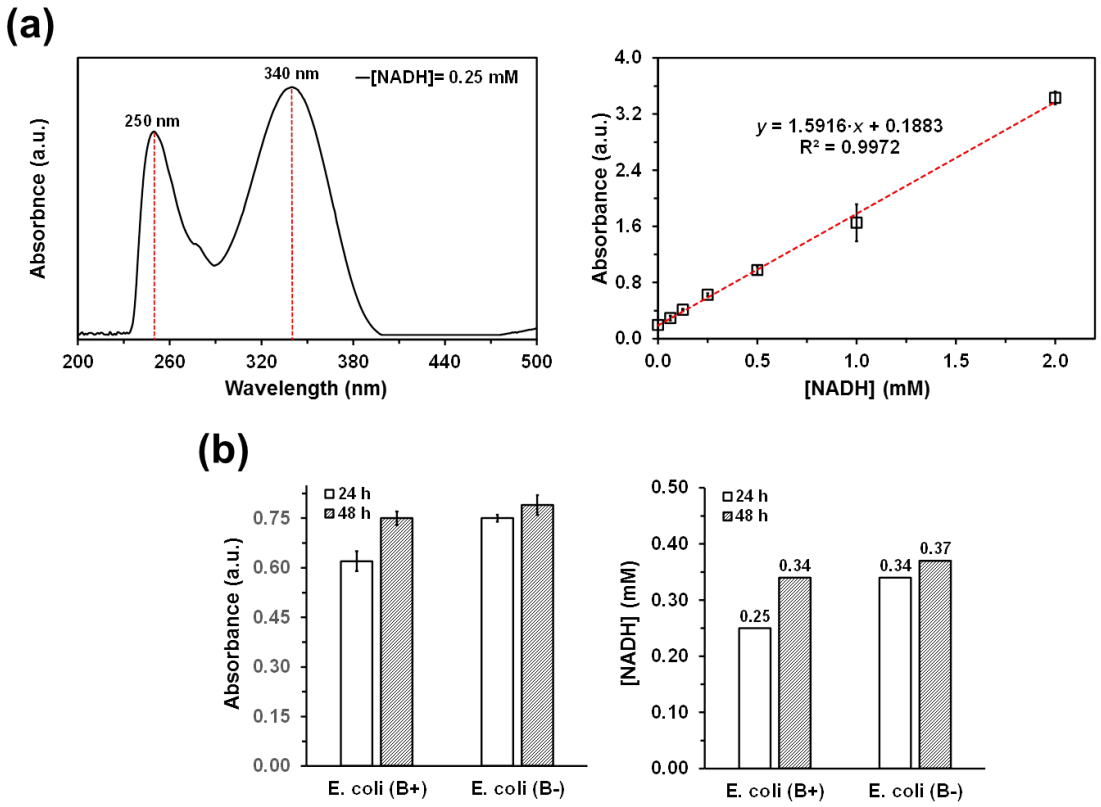

Figure 9. (a) UV-Vis spectrum of a DMEM solution with 0.25 mM NADH (left) and calibration curve obtained by representing the absorbance at λ= 340 nm vs. the concentration of NADH (from 0 to 2 mM) added to a supplemented DMEM solution (right). (b) Absorbance at λ= 340 nm (left) and concentration of extracellular NADH (right) in B+ and B– *E. coli* cultures after 24 and 48 h.

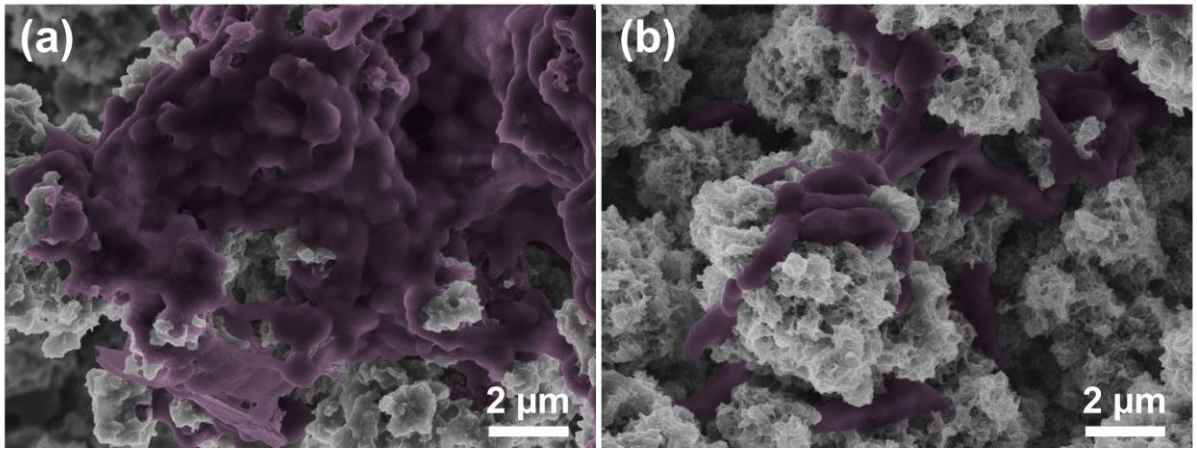

Figure 10. SEM micrographs of i-PP_f/CP^2 incubated by 24 h in B+ (a) and B– (b) *E. coli* cultures.

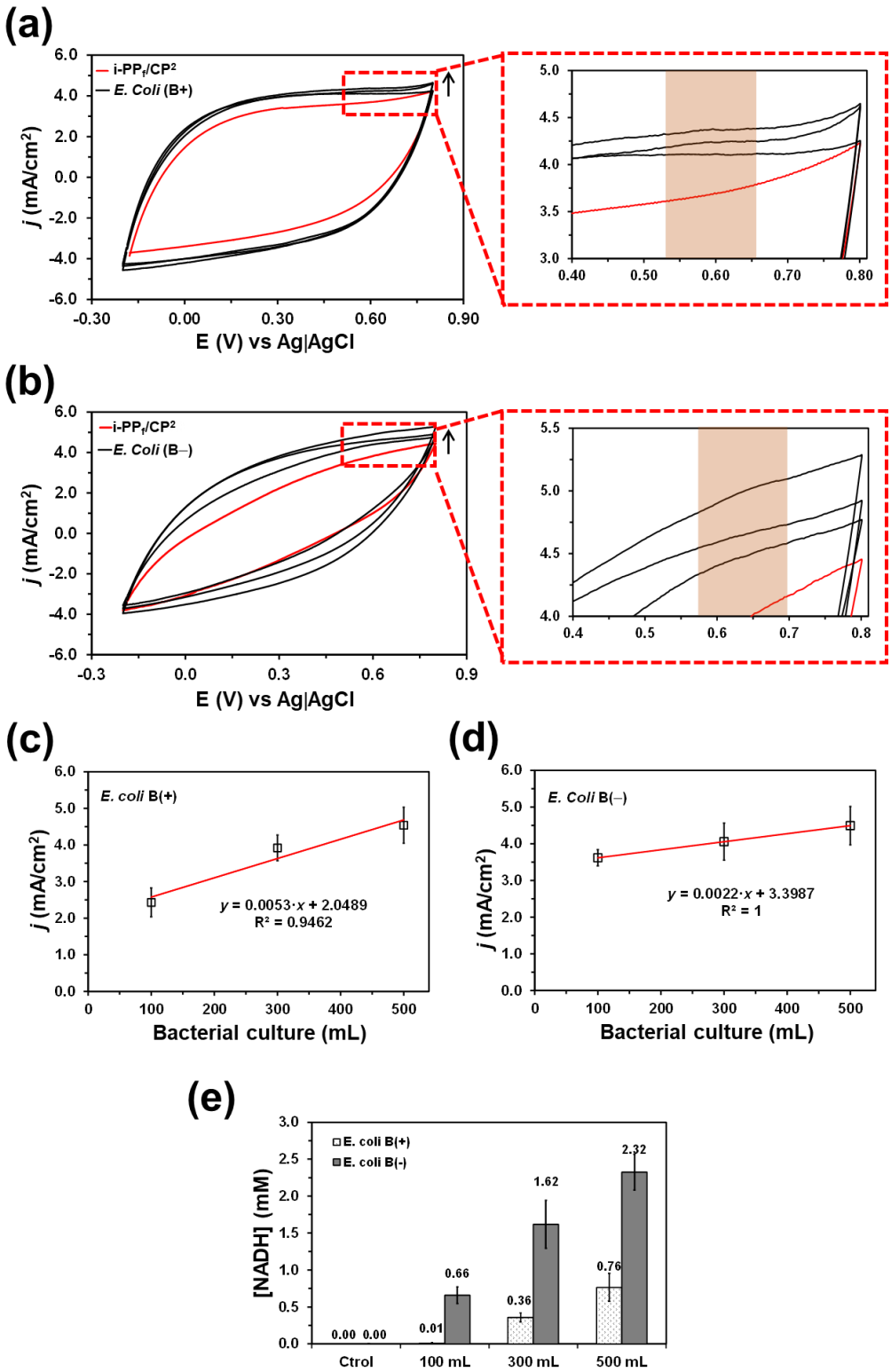

Figure 11. Cyclic voltammograms for i-PP_f/CP^2 in solutions containing the lyophilized extracellular NADH from aerobic *E. coli* (a) B+ and (b) B–metabolism cultured in 100, 300 and 500 mL of supplemented DMEM. The control is represented with the red line. Initial and final potentials: −0.20 V; reversal potential:+ 0.80 V; and scan rate: 50 mV/s. Variation in the NADH current density with the volume of the culture medium for *E. coli* (c) B+ and (d) B–. (e) Concentration of extracellular NADH in *E. coli* B+ and B– cultures as measured by CV in (a) and (b), respectively.

Table 1. Comparison of the i-PP/CP^2 with that reported in reference 14.

	Reference 14	Present work
i-PP films	i-PP powder from conventional industrial production was mixed with 10% w/w NaCl by mechanical stirring and, subsequently, films were obtained by pressing the powder mixture.	i-PP films produced following the standards for biomedical implants (supplied by B Braun Surgical S.A.U.).
Pretreatment of the i-PP films	i-PP/NaCl films were immersed in de-ionized water several cycles of 12 h to produce porous i-PP films.	i-PP films were washed in an ethanol aqueous solution and prepared for functionalization applying an oxygen plasma at pressure of 0.30 mbar during 180 seconds.
Integration of the CP	Independently synthesized PEDOT NPs were integrated by mechanical pressing.	A two-step process: 1) After plasma treatment, a uniform PHMeDOT layer was adhered to i-PP by chemical oxidative polymerization, producing i-PP/CP; and 2) a layer of PEDOT was deposited onto PHMeDOT by electrochemical polymerization, producing i-PP/CP^2.
Performance of the sensor for NADH	LOD: 0.20 mM Current response at 0.2 mM: 20.7μA/cm2	LOD: 0.14 mM Current response at 0.2 mM: 75.9 μA/cm^2

A sensor for bacteria quantification has been implemented in isotatic polypropylene for biomedical implants. The sensor is based on the detection of NADH from bacteria respiration, which is achieved by electropolymerizing poly(3,4-ethylendioxythiophene) on the polypropylene using conducting polymer nanoparticles as polymerization nuclei. The detection limit of the sensor is below the NADH produced by biofilms.

Bacteria quantification

B. G. Molina,* L. J. del Valle, J. Casanovas S. Lanzalaco, M. M. Pérez-Madrigal, P. Turon, E. Armelin, C. Alemán*

Plasma Functionalized Isotactic Polypropylene Assembled with Conducting Polymers for Bacterial Quantification by NADH Sensing

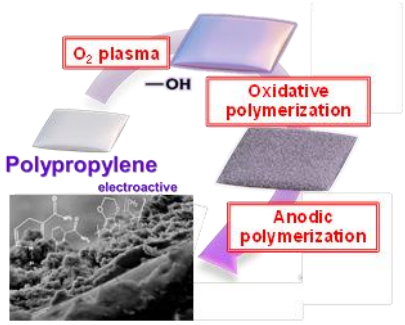

Supporting Information

Plasma Functionalized Isotactic Polypropylene Assembled with Conducting Polymers for Bacterial Quantification by NADH Sensing

B. G. Molina,* L. J. del Valle, J. Casanovas, S. Lanzalaco, M. M. Pérez-Madrigal, P. Turon, E. Armelin, C. Alemán*

Methods

Materials

Isotactic polypropylene (i-PP) films, which were used as a base substrate, were kindly supplied by B Braun Surgical S.A.U. (Rubí, Barcelona, Spain). Hydroxymethyl-3,4-ethylenedioxythiophene (HMeDOT; 95%), 3,4-ethylenedioxythiophene (EDOT; 97%), lithium perchlorate ($LiClO_4$), β-Nicotinamide adenine dinucleotide reduced disodium salt hydrate (NADH; 97%), acetonitrile (99.8%) and phosphate buffered saline (PBS) solution were purchased from Sigma-Aldrich (USA). $LiClO_4$ was stored in an oven at 80 °C before its use in the anodic polymerization. Ammonium persulfate (APS; 98%), hydrochloric acid (37%) and sodium hydroxide were used as received from Panreac Quimica S.A.U. (Spain).

Plasma treatment

For its surface functionalization, i-PP films were previously washed in 30% ethanol aqueous solution. The functionalization was carried out with low pressure radio-frequency (RF) plasma (80 MHz), using a LFG generator 1000 W (Diener Electronic GmbH Co., Germany), and a chamber of 25 dm^3. i-PP films of 6 × 5 cm^2 were placed inside the chamber, the system was purged up to 0.07 mbar of vacuum pressure and, subsequently, filled with oxygen plasma pressure of 0.30 mbar using a gas flow fixed during 180 seconds. The power discharge was of

250 W. After the plasma treatment, all functionalized i-PP films (hereafter named i-PP_f) were stored under vacuum.

Oxidative polymerization

A layer of poly(hydroxymethyl-3,4-ethylenedioxythiophene) (PHMeDOT) was adhered to i-PP_f films by chemical oxidative polymerization. More specifically, i-PP_f films were cut in 0.5 × 1.5 cm^2 samples, which were immersed in 5 mL of a 0.2 M HCl solution with 50 mM HMeDOT (monomer) during 30 min at room temperature and under stirring (250 rpm). After this time, 1 mL of a 0.2 M HCl solution with 60 mM APS was slowly dropped to the solution containing the functionalized film. The reaction was maintained for 24 h at 37 ºC under agitation (80 rpm). After such time, the films were removed, washed three times with milli-Q water, one with acetone and dry at room temperature. Hereafter, the i-PP_f samples with superficial PHMeDOT layer are denoted i-PP_f/CP.

Anodic polymerization

A second layer of conducting polymer (CP) was provided by *in situ* polymerization of EDOT onto the surface of i-PP_f/CP samples, which were previously washed with 0.2 M NaOH. EDOT was polymerized by chronoamperometry (CA) under a constant potential of +1.40 V and adjusting the polymerization charge to 1.0 C. Anodic polymerizations were performed using a VersaStat II potenciostat-galvanostat connected to a computer controlled through a Power Suite Princenton Applied Research program. Experiments were conducted in a three-electrode cell at 25°C, which was filled with 20 mL of a 10 mM EDOT solution in acetonitrile containing 0.1 M $LiClO_4$ as supporting electrolyte. The i-PP_f/CP films (0.5 × 1.5 cm^2) were employed as working electrode, while a platinum wire was used as counter electrode. The reference electrode was an Ag|AgCl electrode containing a KCl saturated aqueous solution

(E^o = 0.222 V at 25 °C). Films made of i-PP_f coated with an internal layer of PHMeDOT and an external layer of PEDOT are identified as i-PP_f/CP^2.

Characterization

X-ray photoelectron spectroscopy (XPS) analyses were used for the detection of chemical species formed on the i-PP surface before and after each modification, the assays were performed in a SPECS system equipped with a high-intensity twin-anode X-ray source XR50 of Mg/Al (1253 eV/1487 eV) operating at 150 W, placed perpendicular to the analyzer axis, and using a Phoibos 150 MCD-9 XPdetector. The X-ray spot size was 650 mm. The pass energy was set to 25 and 0.1 eV for the survey and the narrow scans, respectively. Charge compensation was achieved with a combination of electron and argon ion flood guns. The energy and emission currents of the electrons were 4 eV and 0.35 mA, respectively. For the argon gun, the energy and the emission currents were 0 eV and 0.1 mA, respectively. The spectra were recorded with a pass energy of 25 eV in 0.1 eV steps at a pressure below 6·10 × 9 mbar. These standard conditions of charge compensation resulted in a negative but perfectly uniform static charge. Data processing was performed using the Casa XPS program (Casa Software Ltd., UK) employing C 1s peak as internal reference with a binding energy of 284.8 eV. High-resolution XPS spectra were acquired by Gaussian/Lorentzian curve fitting after S-shape background subtraction. The surface composition was determined using the manufacturer's sensitivity factors.

UV-Vis spectra of the i-PP, i-PP_f, i-PP_f/CP and i-PP_f/CP^2 films were recorded on a UV-Vis-NIR Shimadzu 3600 spectrophotometer equipped with a tungsten halogen visible source, a deuterium arc UV source, a photomultiplier tube UV-vis detector, and an InGaAs photodiode and cooled PbS photocell NIR detectors. Spectra were recorded in the absorbance mode using the integrating sphere accessory (model ISR-3100), the recorded wavelength range being 300-750 nm. The interior of the integrating sphere was coated with a highly diffuse $BaSO_4$

reflectance standard. Measurements, data collection and data evaluation were controlled by the computer software UVProbe version 2.31.

FTIR spectra were recorded on a FTIR Jasco 4100 spectrophotometer through an attenuated total reflection accessory (Top-plate) with a diamond crystal (Specac model MKII Golden Gate Heated Single Reflection Diamond ATR). Samples were evaluated using spectra manager software and, for each sample 64 scans were performed between 4000 and 600 cm^{-1} with a resolution of 4 cm^{-1}.

Samples were characterized by micro-Raman spectroscopy using a commercial Renishaw inVia Qontor confocal Raman microscope. The Raman setup consisted of a laser (at 785 nm with a nominal 300 mW output power) directed through a microscope (specially adapted Leica DM2700 M microscope) to the sample after which the scattered light is collected and directed to a spectrometer with a 1200 lines·mm^{-1} grating. The exposure time was 10 s, the laser power was adjusted to 1% of its nominal output power and each spectrum was collected with 3 accumulations.

Scanning electron microscopy (SEM) was carried out using a Focused Ion Beam Zeiss Neon40 scanning electron microscope operating at 5 kV and equipped with an energy dispersive X-ray analysis (EDX) spectroscopy system.

The surface topography of films was studied by Atomic force microscopy (AFM). Images were obtained with a Molecular Imaging PicoSPM using a NanoScope IV controller under ambient conditions. The tapping mode AFM was operated at constant deflection (*i.e.* vertical constant force with triangular shaped gold-coated silicon nitride). Root mean square roughness (R_q) and profile sections of the images were determined using the statistics application and tools of the NanoScope Analysis software version 1.20 (Bruker), which calculates the average considering all the values recorded in the topographic image with exception of the maximum and the minimum. The scan window sizes were 5×5 μm^2.

Films thickness was obtained using a Dektak 150 stylus profilometer (Veeco, Plainview, NY). Imaging of the films was conducted using the following optimized settings: tip radius = 2.5 μm; stylus force = 3.0 mg; scan length = 1 μm; duration 30 seconds.

Water contact angle measurements were carried out with the water sessile drop method at room temperature. Images of milli-Q water drops (0.5 μL) were recorded after stabilization (10 s) with an OCA 15EC instrument (Data-Physics Instruments GmbH, Filderstadt). The software SCA20 was used to analyses the images. The ellipse method was used to fit a mathematical function to the measured drop contour. Previous to the experiments, the samples were dry under vacuum for 24 hours. For each sample, no less than ten drops were examined.

Electrochemical characterization was carried out by cyclic voltammetry (CV) using an Autolab PGSTAT302N and NOVA software. Experiments were conducted at room temperature in a three-electrode cell filled with a 0.1 M phosphate buffer saline (PBS) solution, pH 7.4, as electrolytic solution, and using the different prepared samples as working electrodes. In all cases, a platinum wire was used as counter electrode, while the reference electrode was an Ag|AgCl electrode containing a KCl saturated aqueous solution (E^0 = 0.222 V at 25 °C). The initial and final potentials were −0.20 V, and the reversal potential was +0.80 V. The ability to exchange charge reversibly (*i.e.* electrochemical activity or electroactivity) and the electrochemical stability (*i.e.* electrostability) were determined through direct measurement of the anodic and cathodic areas in the control voltammograms. For this purpose, 50 consecutive oxidation-reduction cycles were recorded at a scan rate of 50 mV/s.

The loss of electroactivity (LEA, in %) was expressed as:

$$LEA = \frac{\Delta Q}{Q_2} \cdot 100$$

where ΔQ is the difference in the voltammetric charges (in C) between the second and the last cycle, and Q_2 is the voltammetric charge corresponding to the second redox cycle.

The formation of aggregates in medium (i.e. DMEM high glucose supplemented with 2% FBS and 0.2% $NaHCO_3$) in absence and presence of NADH (1 and 10 mM) was examined by dynamic light scattering (DLS). Measurements were performed at room temperature with a NanoBrook Omni Zeta Potential Analyzer from Brookheaven Instruments.

The formation of aggregates in medium (*i.e.* DMEM high glucose supplemented with 2% FBS and 0.2% $NaHCO_3$) in absence and presence of NADH (1 and 10 mM) was examined by dynamic light scattering (DLS). Measurements were performed at room temperature with a NanoBrook Omni Zeta Potential Analyzer from Brookheaven Instruments

Electrochemical detection of NADH

The electrochemical detection of NADH was studied by cyclic voltammetry (CV) using a three-electrode cell and an Autolab PGSTAT302N and NOVA software. The i-PP/CP^2 film and platinum wire were employed as working and counter electrodes, respectively, while the reference electrode was an Ag|AgCl electrode containing a KCl saturated aqueous solution (E^0 = 0.222 V at 25 °C). The initial and final potentials were −0.20 V, and the reversal potential was +0.80 V. Measurements were performed by adding different concentrations of NADH (from 0 to 16 mM) to the electrolytic medium, which was a Dulbecco's modified Eagle medium (DMEM) high glucose supplemented with 2% fetal bovine serum (FBS; pH 8.1) and 0.2% $NaHCO_3$. All the electrochemical results displayed in the article, correspond to the average of three replicates (n=3) for each independent experiment.

NADH size effect

NADH size effect was studied by dynamic light scattering (DLS) using a NanoBrook Omni Zeta Potential Analyzer from Brookheaven Instruments. The measurements were recorded at 25 ºC using a scattering angle of 90º, the effective diameter was obtained from the average of 3 runs with a duration of 120 s each and a previous equilibration time of 60 seconds. The

study was carried out in 2 mL of solution containing 0, 1 or 10 mM NADH prepared in DMEM supplemented with 2% FBS and 0.2% $NaHCO_3$.

Identification of NADH from bacteria respiration reactions

The absorption peak of NADH was identified at λ= 340 nm by recording the UV-Vis spectrum in the absorbance mode (250-800 nm) of a 0.25 mM NADH solution in DMEM high glucose supplemented with 2% FBS (pH 8.1) and 0.2% $NaHCO_3$. The spectrum was acquired on a quart cell (1 mL) using a UV-Vis Cary 100 Bio (Varian) spectrophotometer. Then, a calibration curve was determined by measuring the absorbance at λ= 340 nm with a Synergy HXT multi-mode reader using 0-2 mM NADH solutions in DMEM high glucose supplemented with 2% FBS (pH 8.1) and 0.2% $NaHCO_3$.

In order to prove that bacteria cellular membranes are permeable to NADH, bacteria *Escherichia coli (E. coli*) colony forming units (CFU, 2×10^8 colony) per mL were seeded in DMEM high glucose supplemented with 2% FBS (pH 8.1) and 0.2% $NaHCO_3$. After 24 h, 150 μL were added to 10 mL of the same supplemented medium in sterile vials. The bacteria used for this purpose were ATCC 25922, a biofilm-positive strain (B+), and CECT 101 a biofilm-negative strain (B–). Samples were vortexed for 1 min and incubated at 37 ºC with agitation at 80 rpm for 24 h and 48 h for bacteria growth. The UV absorbance was measured at λ= 340 nm in flat-bottomed 96-well plates with aliquots of culture media (200 μL) using a Synergy HXT multi-mode reader. Results displayed in the article correspond to the average of three replicates (n=3) for each independent experiment.

The electrochemical detection of the different concentrations of NADH from bacteria respiration reactions was performed by CV using a three-electrode cell, as was previously described. 2×10^8 CFU/mL of B+ or B– *E. coli* were seeded in 10 mL of DMEM high glucose supplemented with 2% FBS (pH 8.1) and 0.2% $NaHCO_3$. After 24 h at 37 °C and 80 rpm, the same amount of CFU/mL were added to 100, 300 or 500 mL of the same supplemented

medium in sterile vials. Cultures were maintained at 37 °C and 80 rpm during 24 h, promoting the bacteria growth. Controls were prepared in 100 mL of DMEM supplemented without bacteria but under the same culture conditions. Then, the solutions (*i.e*. the control and B+ or B– *E. Coli* cultured in 100, 300 and 500 mL of DMEM supplemented) were centrifuged at 1×10^4 rpm and 4 °C during 10 minutes. The supernatant was frozen in liquid nitrogen and lyophilized during 4 days. The resulting powders were dissolved in 20 mL of milli-Q water. 15 mL of each solution were used as electrolytic medium in electrochemical trails while 1 mL was analyzed by UV-Vis spectrophotometry.

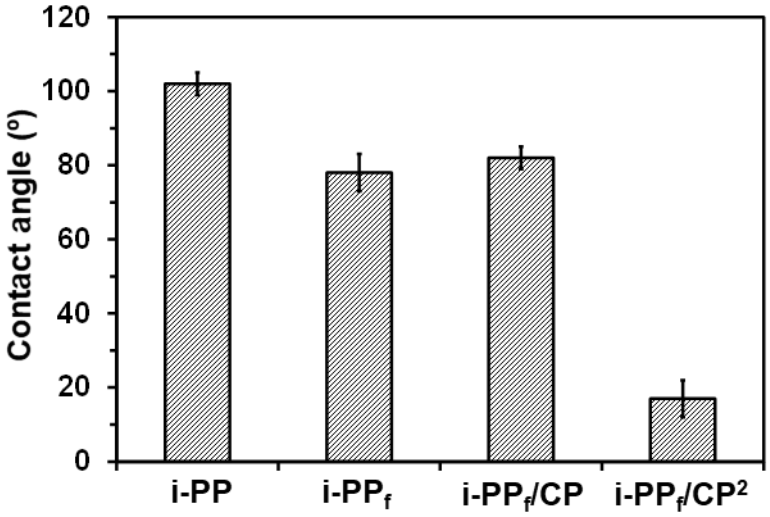

Figure S1. Contact angles for water of i-PP, i-PP$_f$, i-PP$_f$/CP and i-PP$_f$/CP^2.

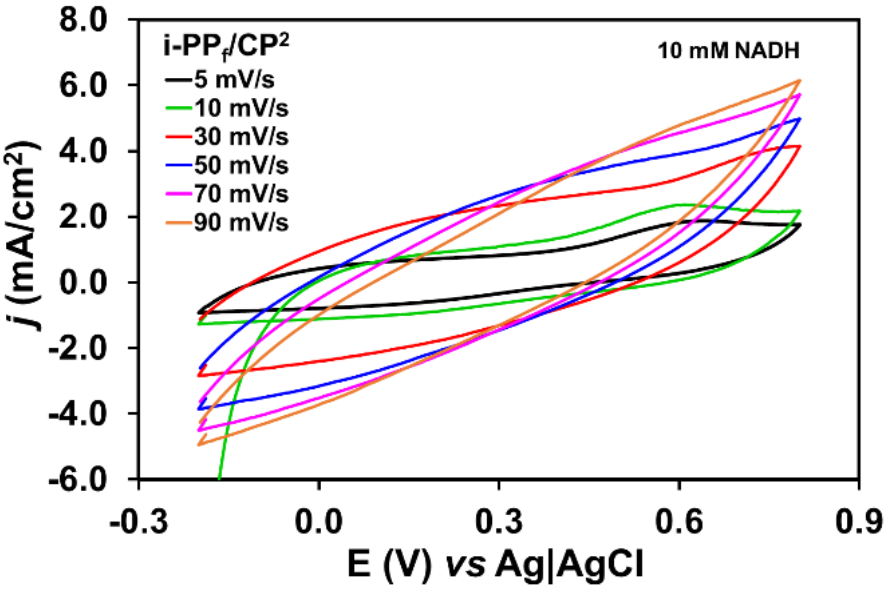

Figure S2. Control voltammograms of i-PP$_f$/CP^2 recorded for 10 mM NADH in PBS (pH 7.4) using different scan rates. Initial and final potentials of −0.20 V; reversal potential of +0.80 V.

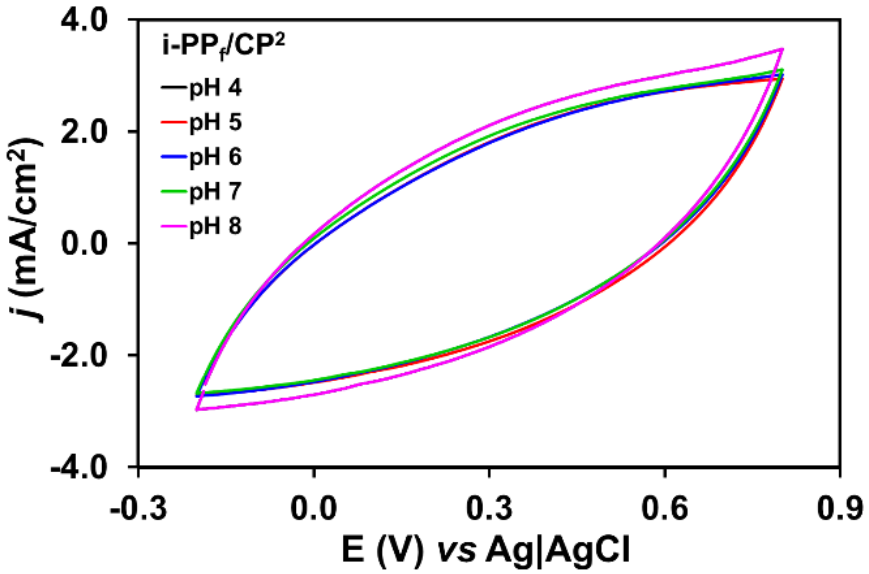

Figure S3. Control voltammograms of i-PP_f/CP^2 recorded in DMEM at different pHs. Initial and final potentials of −0.20 V; reversal potential of +0.80 V and different scan rate: from 50 mV/s.

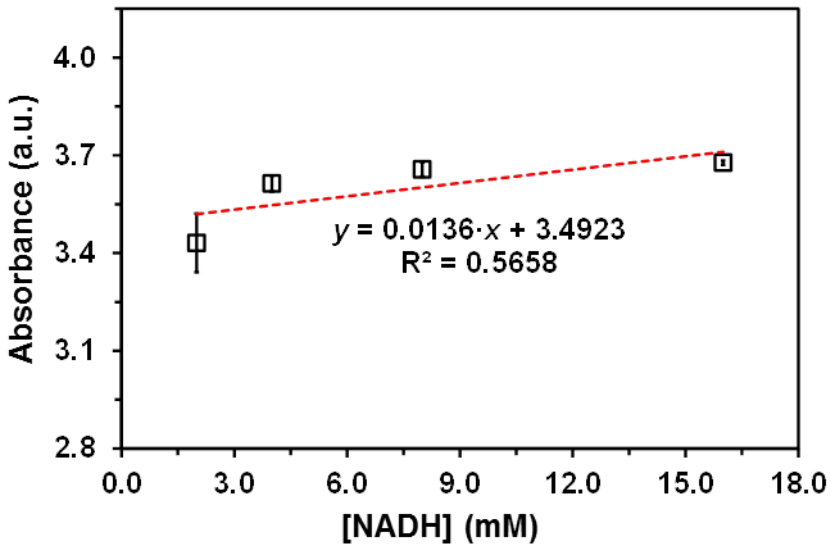

Figure S4. Calibration curve obtained by representing the absorbance at λ= 340 nm *vs.* the concentration of NADH (from 2 to 16 mM) added to a supplemented DMEM solution.

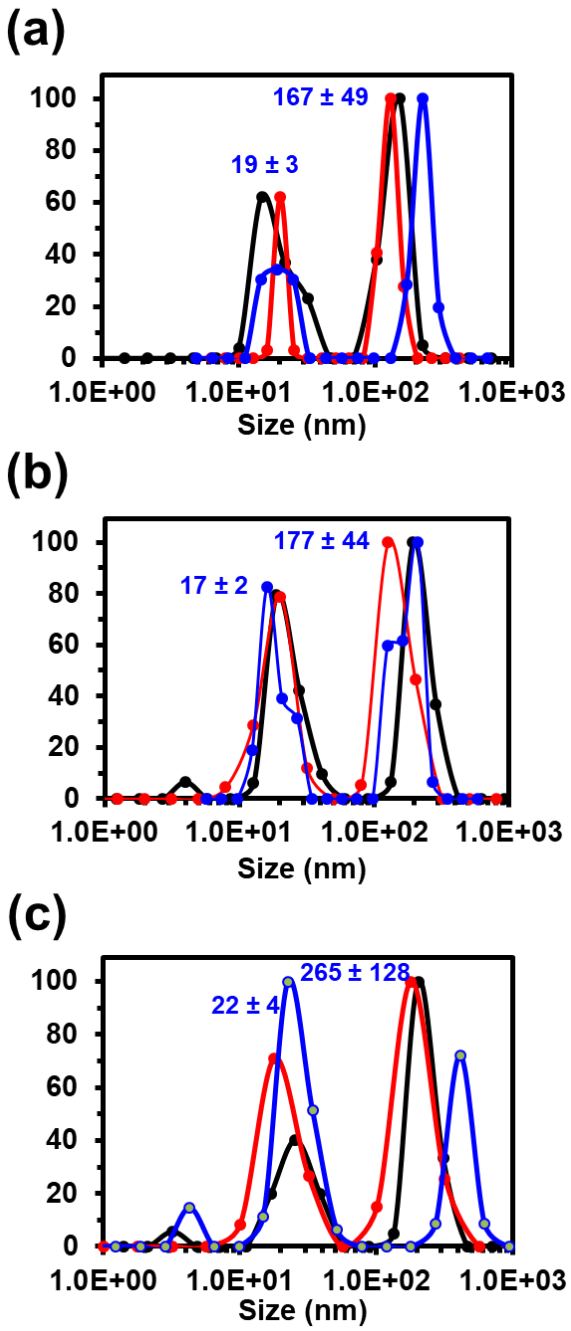

Figure S5. Effective size of formed nanoparticles in DMEM solution: (a) as prepared (*i.e.* in absence of NADH); (b) in presence of 1 mM NADH; and (c) in presence of 10 mM NADH.